

**Acta Biomaterialia**  
**Developing a Neurotrophic Strip: Bridging the Electrode-Neuron Gap in a Bioactive Cochlear Implant**  
--Manuscript Draft--

<b>Manuscript Number:</b>	
<b>Article Type:</b>	Full length article
<b>Keywords:</b>	human pluripotent stem cells; Finite element model; microfluidic device, neurotrophic factor; cochlear implant; neuroelectric interface; stem cell niche; spiral ganglion neurons; controlled release
<b>Corresponding Author:</b>	AKIHIRO JOSEPH MATSUOKA, MDPHD Northwestern University Feinberg School of Medicine Chicago, IL UNITED STATES
<b>First Author:</b>	Kevin T Nella, BS
<b>Order of Authors:</b>	Kevin T Nella, BS Benjamin M Norton, BS Hsiang-Tsun Chang, MS Rachel A Heuer, BS Christian B Roque, BS AKIHIRO JOSEPH MATSUOKA, MDPHD
<b>Abstract:</b>	Although cochlear implant (CI) technology has allowed the patient population to partially restore the sense of hearing over the last few decades, persistent challenges remain, including the deciphering of a rich acoustic signal into an electrical pulse-train signal. Among these challenges, the “electrode-neuron gap” poses a significant obstacle to advancing past the current plateau in CI performance, resulting in limited performance in a noisy background and a poor ability to decode intonation and music. We propose the development of a “neurotrophic strip”-biological interface that doubly preserves endogenous spiral ganglion neurons (SGNs) while precisely directing the growth of neurites arising from transplanted human pluripotent stem cell (hPSC)-derived otic neuronal progenitors (ONPs), toward endogenous SGNs. We hypothesized that Polyhedrin Delivery System PODS®-human brain-derived neurotrophic factor [BDNF] could stably provide an adequate BDNF gradient to hPSC-derived ONPs, thereby facilitating otic neuronal differentiation and directional neurite outgrowth. To test this hypothesis, we first utilized a finite element model to simulate the <i>in vitro</i> BDNF gradient generated by PODS®. For biological verification, we validated the concept of the neurotrophic strip by using a multi-chamber microfluidic device, which mimics the <i>in vivo</i> micro-environment more so than conventional laboratory plates in terms of volume and concentrations of endogenous/exogenous factors. We were able to generate BDNF concentration gradient, enabling survival, neuronal differentiation toward hPSC-derived SGNs, and directed neurite extension of hPSC-derived SGNs. The technique will allow us to further advance our concept of “neurotrophic strip” further in the inner ear by controlling neurite direction of transplanted hPSC-derived ONPs. This proof-of-concept study provides a step toward next-generation bioactive CI technology.

### **Statement of Significance**

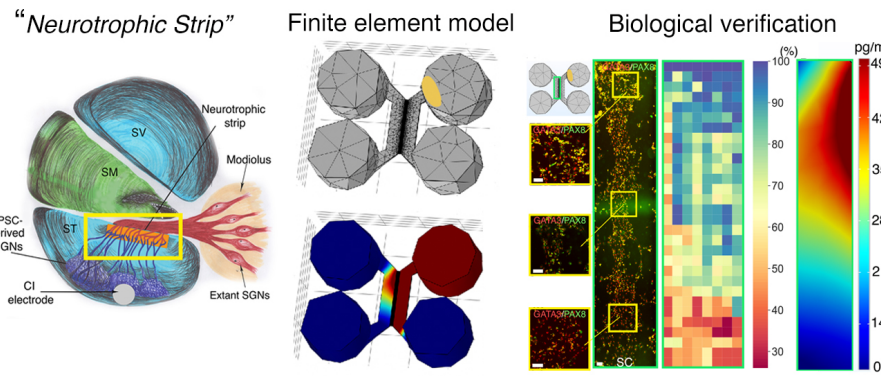
Our study demonstrates the generation of *in vitro* neurotrophin concentration gradient, which enables survival, neuronal differentiation toward auditory neurons, and directed neurite extension of human stem cell-derived auditory neurons. This knowledge is vital for designing a new-generation bioactive cochlear implant because the technique will allow us to control the neurite direction of transplanted stem-cell derivatives in the inner ear. Therefore, this proof-of-concept study provides a step toward next-generation bioactive cochlear implant technology. Finally, this study is the first to present the concept of a ``neurotrophic strip'' in a new-generation bioactive cochlear implant to fill the electrode-neuron gaps, which is the most significant barrier of current cochlear implant technology.

1  
2  
3  
4  
5  
6  
7  
8  
9  
10  
11  
12  
13  
14  
15  
16  
17  
18  
19  
20  
21  
22  
23  
24  
25  
26  
27  
28  
29  
30  
31  
32  
33  
34  
35  
36  
37  
38  
39  
40  
41  
42  
43  
44  
45  
46  
47  
48  
49  
50  
51  
52  
53  
54  
55  
56  
57  
58  
59  
60  
61  
62  
63  
64  
65

## Graphical Abstract

### Developing a Neurotrophic Strip: Bridging the Electrode–Neuron Gap in a Bioactive Cochlear Implant

Kevin T. Nella, Benjamin M. Norton, Hsiang-Tsun Chang, Rachel A. Heuer,  
Christian B. Roque, Akihiro J. Matsuoka



1  
2  
3  
4  
5  
6  
7  
8  
9       Developing a Neurotrophic Strip: Bridging the  
10      Electrode–Neuron Gap in a Bioactive Cochlear Implant  
11  
12

13      Kevin T. Nella<sup>a,b</sup>, Benjamin M. Norton<sup>a</sup>, Hsiang-Tsun Chang<sup>a</sup>, Rachel A.  
14           Heuer<sup>a</sup>, Christian B. Roque<sup>a</sup>, Akihiro J. Matsuoka<sup>a,c,d,e,\*</sup>  
15

16           <sup>a</sup>*Department of Otolaryngology–Head and Neck Surgery, Feinberg School of Medicine,  
17           Northwestern University, Chicago IL, 60611, USA*

18           <sup>b</sup>*Department of Mechanical Engineering, Robert R. McCormick School of Engineering and  
19           Applied Science, Northwestern University, Evanston, IL., USA*

20           <sup>c</sup>*Simpson Querrey Institute, Chicago IL, 60611, USA*

21           <sup>d</sup>*Roxelyn and Richard Pepper Department of Communication Sciences and Disorders,  
22           School of Communication, Northwestern University, Evanston, IL., 60210, USA*

23           <sup>e</sup>*The Hugh Knowles Center for Clinical and Basic Science in Hearing and its Disorders,  
Evanston, IL. 60210, USA*

---

24  
25  
26  
27      **Abstract**  
28

29      Although cochlear implant (CI) technology has allowed the patient population  
30      to partially restore the sense of hearing over the last few decades, persistent chal-  
31      lenges remain, including the deciphering of a rich acoustic signal into an elec-  
32      trical pulse-train signal. Among these challenges, the “electrode-neuron gap”  
33      poses a significant obstacle to advancing past the current plateau in CI per-  
34      formance, resulting in limited performance in a noisy background and a poor  
35      ability to decode intonation and music. We propose the development of a “neu-  
36      rotrophic strip”—biological interface that doubly preserves endogenous spiral  
37      ganglion neurons (SGNs) while precisely directing the growth of neurites arising  
38      from transplanted human pluripotent stem cell (hPSC)-derived otic neu-  
39      ronal progenitors (ONPS), toward endogenous SGNs. We hypothesized that  
40      Polyhedrin Delivery System (PODS®-human brain-derived neurotrophic factor  
41  
42  
43  
44  
45  
46  
47

48  
49  
50      \*Corresponding author: Akihiro J. Matsuoka, Department of Otolaryngology–Head and  
51      Neck Surgery, Feinberg School of Medicine, Northwestern University, 676 North St. Clair  
52      Street Suite 1325, Chicago, IL 60611, USA. E-mail addresses: amatsuok@nm.org, aki-  
53      hiro.matsuoka@northwestern.edu.

54      Email addresses: kevin.nella@northwestern.edu (Kevin T. Nella),  
55           benjamin.norton@northwestern.edu (Benjamin M. Norton), hsiangtsun.chang@gmail.com  
56           (Hsiang-Tsun Chang), racheuer@gmail.com (Rachel A. Heuer), christian.b.roq@gmail.com  
57           (Christian B. Roque), amatsuok@nm.org (Akihiro J. Matsuoka)

1  
2  
3  
4  
5  
6  
7  
8  
9 [BDNF]) could stably provide an adequate BDNF gradient to hPSC-derived  
10 ONPs, thereby facilitating otic neuronal differentiation and directional neurite  
11 outgrowth. To test this hypothesis, we first utilized a finite element model  
12 to simulate the *in vitro* BDNF gradient generated by PODS®. For biological  
13 verification, we validated the concept of the neurotrophic strip by using a multi-  
14 chamber microfluidic device, which mimics the *in vivo* micro-environment more  
15 so than conventional laboratory plates in terms of volume and concentrations  
16 of endogenous/exogenous factors. We were able to generate BDNF concentra-  
17 tion gradient, enabling survival, neuronal differentiation toward hPSC-derived  
18 SGNs, and directed neurite extension of hPSC-derived SGNs. The technique  
19 will allow us to further advance our concept of “neurotrophic strip” further in the  
20 inner ear by controlling neurite direction of transplanted hPSC-derived ONPs.  
21 This proof-of-concept study provides a step toward next-generation bioactive  
22 CI technology.

23

24 *Keywords:* human pluripotent stem cells, finite element model, microfluidic  
25 device, neurotrophic factor, cochlear implant, neuroelectric interface, stem cell  
26 niche, spiral ganglion neurons

27 2010 *MSC:* 74S05, 62P10, 92C20

---

1  
2  
3  
4  
5  
6  
7  
8  
9     **1. Introduction**

10  
11     The cochlear implant (CI), which provides functional restoration in patients  
12     with sensorineural hearing loss, forms a neuro-electronic interface with the pe-  
13     ripheral auditory nervous system [1]. CI technology functions by electrically  
14     stimulating the extant population of auditory neurons (i.e., spiral ganglion neu-  
15     rons [SGNs]). Although CI technology has allowed the patient population to  
16     partially restore the sense of hearing over the last few decades, persistent chal-  
17     lenges remain including the deciphering of a rich acoustic signal into an electrical  
18     pulse-train signal. Among these challenges, the “electrode-neuron gap” poses  
19     a significant obstacle to advancing past the current plateau in CI performance,  
20     resulting in limited performance in noisy background, and poor ability to de-  
21     code intonation and music [2]. The gap exists between the CI electrode and  
22     the target membranes of dendrites in surviving endogenous SGNs [3]. It results  
23     in the requirement of larger CI excitation fields as well as fewer information  
24     channels to the brain, thus contributing to the plateau [2]. Furthermore, the  
25     larger excitation fields lead to current spread, exciting neighboring electrodes  
26     which can no longer be used [4]. Generally the length of the gap spans hundreds  
27     of  $\mu\text{m}$  [5, 6]. Hahnwald et al. demonstrated *in vitro* that even by reducing the  
28     distance from 40 to zero  $\mu\text{m}$  (by growing early postnatal mouse SGN explants  
29     on a microelectrode array), energy needed to elicit a response can be reduced  
30     by up to 20% [4].

31  
32     To resolve the electrode-neuron gap *in vivo*, previous work has introduced  
33     the concept of a bioactive CI (Figure. 1A) [7, 8, 9]. The bioactive CI combines  
34     the current state-of-the-art CI technology with emerging stem cell-replacement  
35     therapy in the inner ear. In this scheme, transplanted human pluripotent stem  
36     cell (hPSC)-derived SGNs bridge the gap between the CI electrode and surviving  
37     endogenous SGNs. To support this notion, several studies suggested artificially-  
38     generated neurotrophin gradients can potentially guide neurite growth from  
39     hPSC-derived neurons. Neurotrophin gradients have been shown to guide hPSC  
40     grafts in spinal cord injury [10], direct growth of endogenous SGNs toward CI  
41  
42

1  
2  
3  
4  
5  
6  
7  
8  
9     31 electrodes in the scala tympani [11], and enable transplanted hPSC derived otic  
10    32 neuronal progenitors (ONPs) to grow neurites toward the modiolus [9]. Al-  
11    33 though promising, previous studies did not observe sufficient directional neurite  
12    34 outgrowth toward endogenous SGNs (i.e., lack of synaptic connections between  
13    35 hPSC grafts and endogenous SGNs), presumably preventing functional recovery  
14    36 of hearing.

15  
16     37 To confront this issue, we propose development of a “neurotrophic strip”—a  
17    38 biological interface that doubly preserves endogenous SGNs while precisely di-  
18    39 recting the growth of neurites, arising from transplanted hPSC-derived ONPs,  
19    40 toward endogenous SGNs. A highlighted yellow-square area in Figure 1A shows  
20    41 a schematic diagram of this concept. Here, the neurotrophic strip (shown in  
21    42 orange square in Figure 1A) stimulates neurite outgrowth both from the hPSC-  
22    43 derived ONPs as well as from endogenous SGNs via a neurotrophic factor gra-  
23    44 dient [12]. While the concept of a neurotrophin gradient for directional axonal  
24    45 growth has been around for a few decades, incorporating neurotrophin gradients  
25    46 into any tissue-engineered scaffold has been extremely challenging due to the  
26    47 lack of self-sustaining neurotrophin delivery methods for optimal neurite elon-  
27    48 gation—the eventual depletion triggers an accelerated decline in neurite growth  
28    49 and the survival of extant SGNs [13, 14, 15]. One major challenge is due to  
29    50 the structually unstable nature of a growth factor protein, which suffer from  
30    51 fragility and thermo-instability under normal physiological conditions both *in*  
31    52 *vitro* and *in vivo*, exhibiting short half-lives typically ranging from minutes to  
32    53 hours [16]. This issue can be overcome by utilizing the polyhedrin delivery  
33    54 system (PODS®)—a crystalline growth factor formulation developed to enable  
34    55 long-term release of growth factors while preventing degradation at the source  
35    56 [17, 18, 19] (Figure 1B). The PODS® technology has adapted viral machinery  
36    57 to encase a chosen growth factor into polyhedrin protein cases. The resultant  
37    58 growth factor co-crystals have slow degradation profiles under physiological con-  
38    59 ditions and, therefore, allow the sustained release of embedded bioactive growth  
39    60 factor protein.

40  
41     61 We reasoned that a neurotrophic strip incorporating PODS® technology can  
42  
43  
44  
45  
46  
47  
48  
49  
50  
51  
52  
53  
54  
55  
56  
57  
58  
59  
60  
61  
62  
63  
64  
65

1  
2  
3  
4  
5  
6  
7  
8  
9  
10  
11  
12  
13  
14  
15  
16  
17  
18  
19  
20  
21  
22  
23  
24  
25  
26  
27  
28  
29  
30  
31  
32  
33  
34  
35  
36  
37  
38  
39  
40  
41  
42  
43  
44  
45  
46  
47  
48  
49  
50  
51  
52  
53  
54  
55  
56  
57  
58  
59  
60  
61  
62  
63  
64  
65

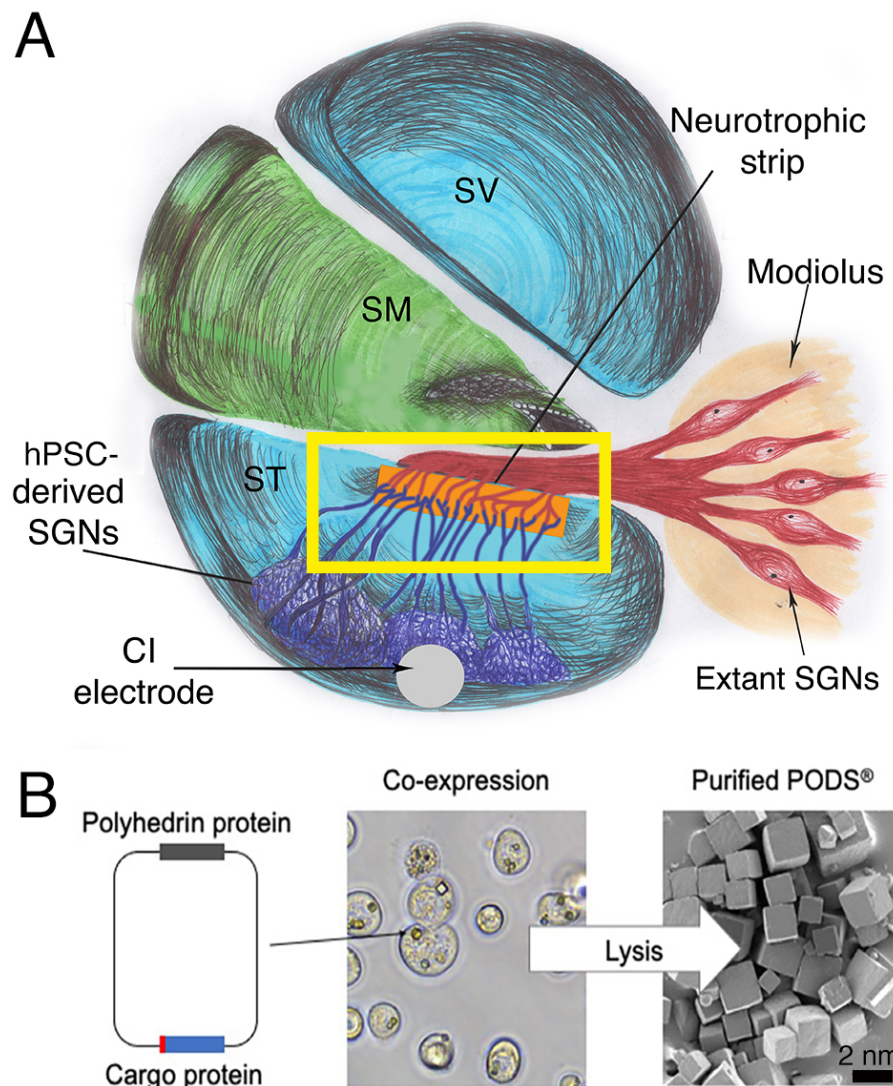


Figure 1: (A): A next-generation bioactive CI and a neurotrophic strip. The neural network in this scheme consists of a CI electrode, transplanted stem cell-derived SGNs, the neurotrophic strip, and extant/endogenous SGNs (red). Note that neuronal connection is largely absent with hair cells (not shown). (B): Polyhedrin Delivery System (PODS)®. PODS® crystals are cubic protein co-crystals produced by Sf9 cells (a clonal isolate of *Spodoptera frugiperda* Sf21 cells [IPLB-Sf21-AE], in which the polyhedrin protein and a second protein are co-expressed). This second protein is termed as the active, or cargo protein (Figure 1B, left). Inside the Sf9 cells, polyhedrin proteins self-assemble into cubic crystals (Figure 1B, center) while the active protein, tagged with a short peptide sequence, binds to the growing polyhedrin crystal purified by simple cell lysis and washes to remove cell debris (Scanning electron micrograph, Figure 1B, right).

1  
2  
3  
4  
5  
6  
7  
8  
9     62 establish a neuronal network between transplanted hPSC-derived ONP grafts  
10    63 and extant SGNs in the inner ear. More specifically, we hypothesized that  
11    64 PODS®-human neurotrophin system could stably provide an adequate neu-  
12    65 rotrophin gradient to hPSC-derived ONPs, thereby facilitating otic neuronal dif-  
13    66 ferentiation and directional neurite outgrowth. To test this hypothesis, we first  
14    67 utilized a finite element model (FEM) to simulate the *in vitro* neurotrophin gra-  
15    68 dient generated by PODS®. In this study, we focus on the role of BDNF—the  
16    69 most studied of the neurotrophins in the inner ear, and also the most important  
17    70 one for the functional recovery of damaged SGNs [20]. For biological verifi-  
18    71 cation, we validated the concept of the neurotrophic strip by using a multi-  
19    72 chamber microfluidic device, which mimics the *in vivo* micro-environment more  
20    73 so than conventional laboratory plates in terms of volume and concentrations  
21    74 of endogenous/exogenous factors [21].  
22  
23  
24  
25  
26  
27  
28  
29  
30

31     75 **2. Materials and Methods**  
32  
33  
34

35     76 *2.1. Polyhedrin delivery system*  
36  
37  
38  
39  
40  
41  
42  
43  
44  
45

46     77 The Polyhedrin Delivery System (PODS®-human BDNF [hBDNF]) (Cell  
47    78 Guidance Systems, Cambridge, United Kingdom) was used for a sustained-  
48    79 release source of hBDNF. PODS®-hBDNF utilizes the polyhedrin protein formed  
49    80 by *Bombyx mori*, an insect from the moth family *Bombycidae*. A cargo pro-  
50    81 tein (i.e., hBDNF) is co-expressed within the polyhedrin and is slowly released  
51    82 with degradation of the PODS® crystals by cell-released proteases (Figure  
52    83 1B)[9, 18, 22].  
53  
54  
55  
56  
57  
58  
59  
60  
61  
62  
63  
64  
65

66     84 *2.2. Human pluripotent stem cell culture using multi-channel microfluidic device*  
67  
68  
69  
70  
71  
72  
73  
74  
75  
76  
77  
78  
79  
80  
81  
82  
83  
84  
85  
86  
87  
88  
89

80     Human embryonic stem cells (hESCs: H7 and H9, passages number 25–35)  
81    and were obtained from WiCell Research Institute (Madison, Wisconsin, USA).  
82     Human induced pluripotent stem cells (hiPSCs: TC-1133HKK, passage num-  
83    ber 22–35) were generated from human CD34+ cord blood cells using the four  
84    Yamanaka factors at Lonza (Walkersville, Maryland [MD], USA). The hiPSC  
85  
86  
87  
88  
89

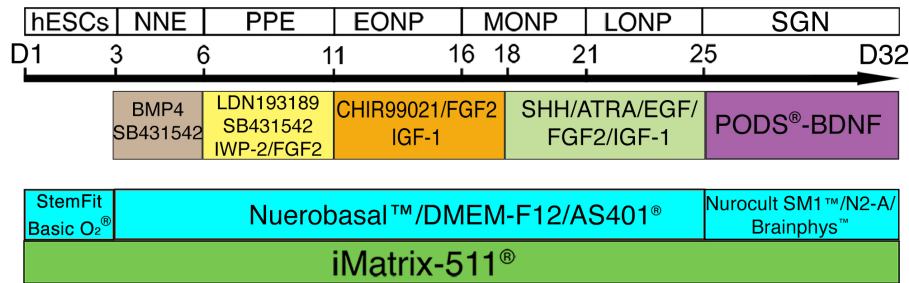


Figure 2: Overview of otic neuronal differentiation protocol for hPSCs. Please see detail in [8, 9, 23, 24] and the Supplemental Data. Each developmental stage is shown at the top, with key treatments shown below. NNE: nonneuronal ectoderm; PPE: preplacodal ectoderm; EONP: early-stage otic neuronal progenitor; MONP: mid-stage otic neuronal progenitor; LONP: late-stage otic neuronal progenitor; BMP4: bone morphogenetic protein 4; SHH: Sonic hedgehog; ATRA: all-trans retinoic acid; EGF: epidermal growth factor; IGF-1: insulin-like growth factor-1; FGF2: fibroblast growth factor 2; N2B27-CDM: chemically defined medium containing N2 and B27 supplements.

cell line (TC-1133HKK) was kindly provided by Healios K.K. (Tokyo, Japan). hPSC-derived ONPs were generated based on our previously established protocol (Supplemental Data) [8, 9, 23, 24]. A stepwise series of ligands and growth factors was added to a neuronal induction medium to promote hPSC differentiation toward the late-stage ONP lineage—mitotic progenitor population that generates the SGNs. (Figure 2).

Microfluidic devices provide a platform for specifically evaluating axonal regeneration [25]. Here, multi-chamber microfluidic devices, Xona™ Microfluidics XC150 and XC450 (Xona™ Microfluidics, Research Triangle Park, North Carolina, USA), were used for computational calculation and biological validation (Figure 3A–B). The Xona™ device allows for neurites to grow toward growth factors while limiting migration of derived ONP cell bodies due to specific dimensions of the device.

The devices were washed and coated with poly-L-ornithine (PLO, 20 µg/mL in H<sub>2</sub>O, Sigma-Aldrich, St. Louis, Missouri [MO], USA) and recombinant laminin-511 (iMatrix-511, 0.5 mg/mL, Nacalai USA, San Diego, California [CA],

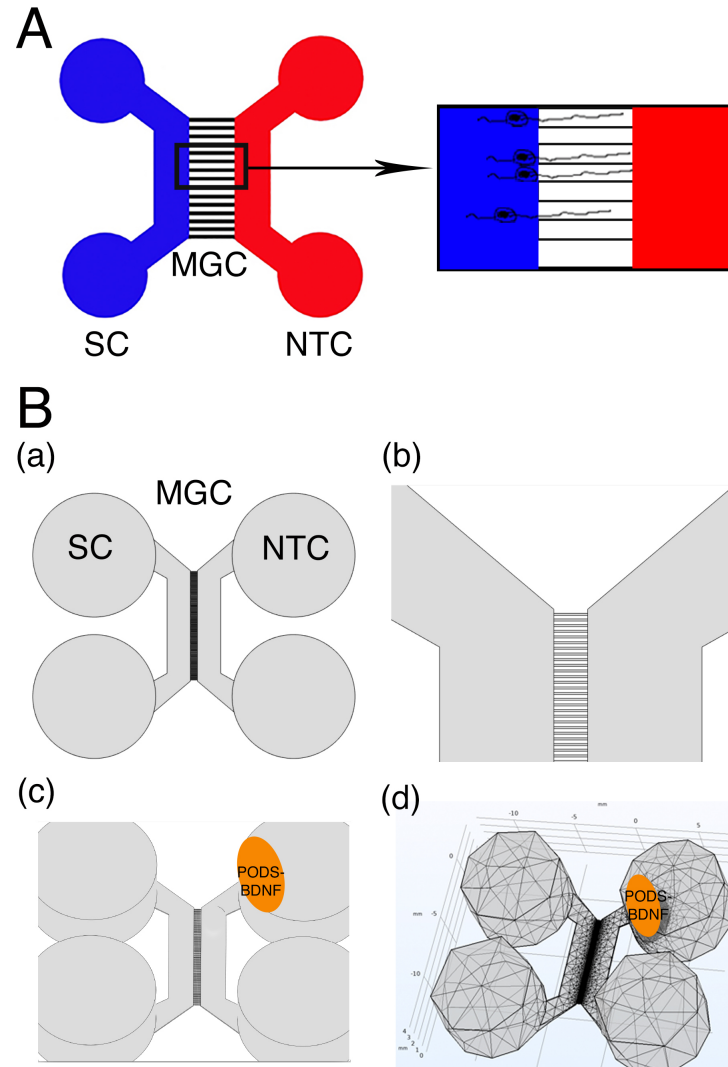


Figure 3: (A): Schematic specification of a Xona<sup>TM</sup> Microfluidics XC 450. Two main channels (Somal compartment (SC) and Neurotrophin compartment (NTC)) on either side are connected by a micro-groove channel (MGC) spanning 450  $\mu\text{m}$  with a width of 10  $\mu\text{m}$  (black square). The somal compartment contains hPSC-derived late-stage ONPs (shown in black), while the neurotrophin compartment contains secreted factors (i.e., BDNF) that are released from PODS®-hBDNF ceystals. (B):(a) Xona<sup>TM</sup> Microfluidics XC450 device geometry, created at a 1:1 scale in Autodesk Inventor®, in which the diffusion profile of BDNF was tested. (b) Detail of the microchannels in the middle part of the Xona<sup>TM</sup> Microfluidics XC450. (c) Xona<sup>TM</sup> Microfluidics XC450 device showing the optimal area to place PODS® containing recombinant hBDNF (yellow ellipse-shaped area). (d): Mesh geometry of the Xona<sup>TM</sup> XC450 generated with Autodesk Inventor, depicting the localized volume of PODS®-hBDNF (1  $\mu\text{L}$ ) as an ellipse-shaped disk (black circle, the device is seen from the bottom to show the exact location of the disk).

1  
2  
3  
4  
5  
6  
7  
8  
9       106 USA) according to the manufacturer-outlined protocol. Next, approximately  
10      107  $1.75 \times 10^5$  cells (in 20  $\mu\text{L}$  of media) were added to the top and bottom left well  
11      108 (i.e., the total amount of  $3.5 \times 10^5$  hPSC-derived ONPs were added).

12  
13       109 PODS<sup>®</sup>-hBDNF were placed in the top right well of the neurotrophin com-  
14      110 partment (Figure 3A–B) to generate a BDNF concentration gradient for di-  
15      111 rectional neurite growth. hPSC-derived ONPs were cultured for 7 days in a  
16      112 Xona<sup>TM</sup> device to induce otic neuronal differentiation. Note that due to our  
17      113 use of the microfluidic device, high-density cell cultures were induced to facili-  
18      114 tate molecular studies as well as the generation of a more biologically relevant  
19      115 neuronal phenotype (i.e., otic lineage) [25]. Media was topped off daily after  
20      116 imaging (from 20-40  $\mu\text{L}$  per well).

21  
22       117 *2.3. Three-dimensional finite element model*

23  
24       118 We used finite element analysis (FEA) to simulate the BDNF concentra-  
25      119 tion gradient in a multi-chamber microfluidic device. FEA is a numerical tech-  
26      120 nique, which approximates mathematical solutions to partial differential equa-  
27      121 tions (PDEs) that appropriately simulate complex real-world problems. In this  
28      122 study, the finite element model allowed us to predict the concentration gradient  
29      123 with respect to time in the multi-chamber microfluidic device dependent on the  
30      124 number of PODS<sup>®</sup>-hBDNF introduced into the system. To solve the finite ele-  
31      125 ment model, we used COMSOL<sup>®</sup> Multiphysics (version 5.6 [released on Novem-  
32      126 ber 11, 2020], COMSOL, Inc., Burlington, Massachusetts [MA], USA), which is  
33      127 a finite element method solution tool in engineering and scientific research com-  
34      128 putations. We used the Xona<sup>TM</sup> Microfluidics XC450 geometry for this compu-  
35      129 tation based on the data in our previous study [9] as well as sustained-release  
36      130 kinetics for PODS<sup>®</sup>-hBDNF determined from an ELISA study (see next subsec-  
37      131 tion). Device geometry was generated at a 1:1 scale using Autodesk<sup>®</sup> Inventor  
38      132 2019.0.2 (Autodesk, Mill Valley, CA, USA) (Figure 3B). Based on COMSOL<sup>®</sup>  
39      133 Multiphysics 5.6 and MATLAB R2020b (9.9.0.1495850, September 30, 2020,  
40      134 MathWorks, Natick, CA, USA), the calculation was implemented on a high-  
41      135 performance desktop computer platform equipped with a CPU (AMD Ryzen

1  
2  
3  
4  
5  
6  
7  
8  
9       136 Threadripper 3990X 64-Core, 128-Thread @ 4.3 GHz) with 64 GB RAM, and  
10      137 two GPU cards (NVIDIA GeForce RTX 3080Ti,12GB 384-bit GFF6X Graphics  
11      138 card).

12  
13  
14       139 *2.4. Enzyme-linked immunosorbent assay for brain-derived neurotrophic factor*

15       140 In order to determine the release and degradation kinetics of PODS®-  
16      141 hBDNF, an experiment measuring concentrations at multiple time points was  
17      142 performed. To measure the concentration of hBDNF secreted from PODS®-  
18      143 hBDNF crystals, the culture media from both a control and an experimental  
19      144 condition were collected at each time point and immediately stored at -80°C  
20      145 before running an enzyme-linked immunosorbent assay (ELISA). The same  
21      146 method was applied to measure the degradation of recombinant hBDNF protein  
22      147 with a carrier protein (Bovine Serum Albumin [BSA]) (#248-BDB-050, R&D  
23      148 Systems, Minneapolis, Minnesota, USA). Experimental conditions were culture  
24      149 media enriched with 10% fetal bovine serum (FBS) (Thermo Fisher Scientific,  
25      150 Waltham, MA, USA). All samples were quantified with a BDNF ELISA kit (#  
26      151 BGK23560; PeproTech, Rocky Hill, New Jersey, USA), and the results were an-  
27      152 alized with a Synergy HTX Multi-Mode Reader (BioTek, Winocski, Vermont,  
28      153 USA) at a 450 nm wavelength, as instructed by the manufacturer. Release  
29      154 and degradation kinetics were then calculated using a MATLAB Curve Fitting  
30      155 Toolbox (MathWorks, Natick, CA, USA).

31  
32       156 *2.5. Sodium dodecyl sulphate-polyacrylamide gel electrophoresis*

33       157 Sodium dodecyl-sulfate polyacrylamide gel electrophoresis (SDS-PAGE) is  
34      158 commonly used as a method to separate proteins with molecular masses be-  
35      159 tween 5 and 250 kDa [26], the range of which is suitable for detecting human  
36      160 BDNF protein (molecular weight [MW]: 14kDa [27]) and polyhedrin (MW: ~29  
37      161 kDa [22]). In this study, SDS-PAGE was used to assess the molar ratio of  
38      162 BDNF to polyhedrin in each sample. Briefly, each protein sample was diluted  
39      163 in deionized water or 12.5 pH NaOH solution and mixed with 6x Laemmli sam-  
40      164 ple buffer (Bio-Rad Laboratories, Inc., Des Plaines, Illinois [IL], USA) contain-  
41      165 ing 2-mercaptoethanol and heated at 100°C for 5 to 20 minutes. Samples were

1  
2  
3  
4  
5  
6  
7  
8  
9       166 then loaded into precast Mini-PROTEAN TGX 4-15% polyacrylamide mini-gels  
10      167 (Bio-Rad Laboratories, Inc., Des Plaines, IL, USA). Then, 5 mL of Precision  
11      168 Plus Protein Kaleidoscope Prestained Protein Standards (Bio-Rad Laborato-  
12      169 ries, Inc., Des Plaines, IL, USA) were loaded in each gel run. Electrophoresis  
13      170 was performed at room temperature for approximately 90 minutes using a con-  
14      171 stant voltage (100V) in 1x solution of Tris-Glycine-SDS electrophoresis buffer  
15      172 (Bio-Rad Laboratories, Inc., Des Plaines, IL, USA) until the dye front reached  
16      173 the end of the 60 mm gel. After electrophoresis, the mini-gels were rinsed  
17      174 with deionized water 3 times for 5 minutes and were subsequently incubated  
18      175 in SimplyBlue™ SafeStain (ThermoFisher Scientific, Waltham, MA, USA) for  
19      176 one hour at room temperature with gently agitation. Images obtained from gels  
20      177 were analyzed using ImageJ 1.53g (December 4, 2020, the National Institutes of  
21      178 Health, Bethesda, MD, USA [28]). These data were applied to the COMSOL®  
22      179 Multiphysics model to accurately predict the amount of hBDNF released from  
23      180 PODS®-hBDNF. SDS-PAGE was performed according to the manufacture's  
24      181 technical guide (Bio-Rad Laboratories, Inc., Des Plaines, IL, USA).

35      182 *2.6. Western Blot*  
36

37      183 The identity of the BDNF protein detected by SDS PAGE was verified by  
38      184 western blot (Bio-Rad Laboratories, Inc., Des Plaines, IL, USA). Briefly, the  
39      185 polyvinylidene difluoride (PVDF) membrane was prepared in methanol for 30  
40      186 seconds before soaking in 1x Tris-Glycine-Methanol transfer buffer for 10 min-  
41      187 utes. Wet transfer was performed at 4°C for approximately 60 minutes using a  
42      188 constant voltage (100V) in 1X solution of Tris-Glycine-Methanol transfer buffer.  
43      189 After transfer, the membrane was briefly rinsed with 1X Tris-buffered saline  
44      190 Tween-20 (TBST) and was subsequently blocked in 5% BSA in TBST for 24  
45      191 hours at 4°C with gentle agitation. The membrane was then rinsed with 1x  
46      192 TBST before incubating in BDNF polyclonal antibody (ThermoFisher Scien-  
47      193 tific, Waltham, MA, USA) diluted to 1:1500 in 1% BSA in TBST for 24 hours at  
48      194 4°C with gentle agitation. Following incubation, the membrane was rinsed in 1x  
49      195 TBST 5 times for 5 minutes to remove unbound primary antibody. Then, the

1  
2  
3  
4  
5  
6  
7  
8  
9       membrane was incubated in Goat anti-Rabbit IgG (H+L) horseradish peroxi-  
10      dase (HRP) conjugated secondary antibody (ThermoFisher Scientific, Waltham,  
11      MA, USA) diluted to 1:5000 in 1% BSA in TBST for one hour at room tem-  
12      perature with gentle agitation. Following incubation, the membrane was rinsed  
13      in 1x TBST 5 times for 5 minutes to remove unbound secondary antibody.  
14      For sensitive detection, the membrane was treated with Pierce™ ECL Western  
15      Blotting Substrate (ThermoFisher Scientific, Waltham, MA, USA), and visual-  
16      ized using an Azure 600 Digital Imager (Azure Biosystems, Dublin, CA, USA).  
17      Electrophoresis buffer for sample condition and run condition was summarized  
18      in Supplementary Table S1.  
19  
20  
21  
22  
23  
24

25           2.7. *Immunocytochemistry and image acquisition*  
26  
27        Glass coverslips (Corning Inc., Corning, New York, USA) were coated with  
28        poly-d-lysine (PDL) (#A3890401, ThermoFisher Scientific, Waltham, MA, USA)  
29        and poly-ornithine (PLO) (# A-004-C, MilliporeSigma, St. Louis, MO, USA)  
30        affixed to a somal compartment as per the manufacturer's instructions. A to-  
31        tal of 100,000 dissociated hPSC-derived ONPs were plated onto a somal com-  
32        partment of the device. On Day 7, 4% (w/v) paraformaldehyde (PFA) (Ther-  
33        moFisher Scientific, Waltham, MA, USA) was added to the compartments for  
34        20 minutes to fix the cells. ICC was used to stain for GATA3, PAX8, and  
35        beta-III tubulin. These three proteins have shown to appropriately characterize  
36        ONPs in our previous studies [8, 9, 24]. Following PBS wash, cultures were  
37        blocked with 5% BSA at room temperature for 1 hour. Cultures were then  
38        incubated overnight at 4°C on a shaker plate in primary antibody solution us-  
39        ing Rabbit anti-Beta-III-Tubulin (1:100, Abcam, Cambridge, MA, USA), Goat  
40        anti-PAX8 (1:500, Abcam, Cambridge, MA, USA), and Mouse anti-GATA3  
41        (1:500, R&D Systems, Minneapolis, MN, USA). Following PBS washes, cultures  
42        were incubated at room temperature for 90 minutes on a shaker plate in sec-  
43        ondary antibody solution composed of Alexafluor647 anti-Rabbit (1:1000, Ther-  
44        moFisher Scientific, St. Louis, MO, USA), Alexafluor488 anti-Goat (1:1000,  
45        ThermoFisher Scientific, St. Louis, MO, USA), and Alexafluor594 anti-Mouse  
46  
47  
48  
49  
50  
51  
52  
53  
54  
55  
56  
57  
58  
59  
60  
61  
62  
63  
64  
65

1  
2  
3  
4  
5  
6  
7  
8  
9        226 (1:1000, ThermoFisher Scientific, St. Louis, MO, USA) in 1% BSA. Following  
10      227 PBS -/- washes, cultures were incubated with DAPI for 20 minutes (300 nM,  
11      228 ThermoFisher Scientific, St. Louis, MO, USA). Secondary antibody controls  
12      229 were performed each time multiple primary antibodies were used [29]. Label-  
13      230 ing controls (detection controls) were performed for a sample from each batch  
14      231 of hPSC culture [29]. See Supplementary Figure S1 for exemplary figures for  
15      232 these control conditions. Results were imaged using a Nikon Ti2 Widefield  
16      233 Laser Microscope System (Nikon, Tokyo, Japan). Phase-contrast images were  
17      234 captured on a Nikon Eclipse TE2000-U inverted microscope (Nikon, Tokyo,  
18      235 Japan). All fluorescence images were acquired on a Zeiss LSM 510 META laser-  
19      236 scanning confocal microscope (Carl Zeiss, Oberkochen, Germany), a Nikon Ti2  
20      237 laser laser-scanning confocal microscope (Nikon, Tokyo, Japan), or a Leica SP5  
21      238 laser-scanning confocal microscope (Leica, Welzlar, Germany). Observers were  
22      239 blinded to the conditions during imaging and tracing. In general, the images  
23      240 were processed with a Image J ver. 1.53j or Matlab R2020b. Further detail on  
24      241 image acquisition and quantification of fluorescent-positive cells can be found  
25      242 in the Supplemental Data.

36  
37        243 *2.8. Preferred cell orientation analysis*

38  
39        244 Collective cell migration, where cells organized in a tightly connected fashion  
40      245 migrate as cohesive structures, is a critical biological process to highlight the  
41      246 neurotrophin diffusion gradient profile [30]. To evaluate this process, time-lapse  
42      247 acquisition of images of the Xona™ device was performed using an inverted  
43      248 microscope (Nikon Eclipose TS100, Tokyo, Japan) at Day 1, 3, 5, and 7. Due  
44      249 to the high cell density required for hPSC-ONPs to survive in a somal com-  
45      250 partment of a Xona™ device, images were not amenable to manual analysis in  
46      251 most of the cases. To circumvent this problem, we performed a series of image  
47      252 pre-processings that are mainly based on modified binarization-based extraction  
48      253 of alinement score methods with some modifications [31]. We used MATLAB Im-  
49      254 age Processing Toolbox R2020b (version 9.9.0.1495850, September 30th, 2020,  
50      255 Mathworks, Natick, MA) for analysis. Please see Supplementary Figure S2 for

1  
2  
3  
4  
5  
6  
7  
8  
9     256 further detail. The analysis of directional data in general represents a particu-  
10    257 lar challenge: There is no reason to designate any particular point on the circle  
11    258 as zero, as it is somewhat arbitrary depending on where one sets a coordinate  
12    259 [32, 33]. In this study, we used polar coordinates to determine the directionality  
13    260 of preferred cell orientation. For this analysis, we again used MATLAB Image  
14    261 Processing Toolbox R2020b. See detailed discussion on how we determined the  
15    262 preferred cell orientation in Supplementary Figure S3.

20  
21     263 *2.9. Neurite alignment vector assay, neurite growth assay and cell migration*  
22         264 *assay*

23  
24     265 The microfluidic device allowed us to culture hPSC-derived ONPs in a po-  
25    266 larized manner and to directly isolate/analyze neurites. To evaluate the neurite  
26    267 projection into the neurotrophin compartment by derived otic neurons cultured  
27    268 in the somal compartment, we performed a neurite alignment vector assay. We  
28    269 also evaluated the length of neurites that grew from hPSC-derived ONPs. For  
29    270 these purposes, hPSC-derived ONPs were cultured in a Xona<sup>TM</sup> XC450 for  
30    271 seven days and then immunostained with *beta*-III tubulin and DAPI. We used  
31    272 two ImageJ plug-in toolkits, NeuriteTracer and NeuronJ, to assess neurite align-  
32    273 ment and neurite growth [34, 35]. Due to the bipolar nature of hPSC-derived  
33    274 ONPs/SGNs, we measured the two longest neurites from the cells [24, 36].  
34    275 Please see Supplementary Figure S4 for detailed description of this analysis.  
35    276 We used hPSC-derived ONPs cultured with 800,000 PODS®-hBDNF as a pos-  
36    277 itive control. The number 800,000 was chosen based on our FEM in that there  
37    278 was no neurotrophin gradient in a somal compartment. As a negative control,  
38    279 we used 20 ng/mL of recombinant human BDNF. To evaluate cell migration  
39    280 across a microgroove channel, we performed cell migration analysis. We manu-  
40    281 ally counted the number of ONPs that migrated from the somal compartment  
41    282 into the microchannels, as well as the neurotrophin compartment.

42  
43     283 *2.10. Statistical analysis*

44  
45     284 When appropriate, and as indicated in each figure, statistical analysis was  
46    285 performed. Experimental values are typically expressed as mean and standard

1  
2  
3  
4  
5  
6  
7  
8  
9        error (SE). The majority of the statistical analyses were performed with Python  
10      3.9.6. (Python Software Foundation, Wilmington, Delaware, USA). The follow-  
11      ing libraries were used for the statistical analysis: Scipy, Numpy, Matplotlib,  
12      and Seaborn [37, 38, 39]. Normal distributions were assumed unless mentioned  
13      otherwise.  $P$  values smaller than 0.05 were considered statistically significant.  
14      For circular statistics, we derived the sample mean vector and its polar coor-  
15      dinate. Mean and confidence intervals were calculated. We chose confidence  
16      coefficient,  $Q$ , e.g.  $Q = 0.95$ . To analyze the axial nature of data, especially to  
17      compute the mean vector angle, we doubled each angle and reduced the mul-  
18      tiples modulo  $360^\circ$ . Please see detailed discussion in Supplementary Figure S3  
19      and S5. The Rayleigh test of uniformity and V-test were performed to deter-  
20      mine whether the samples differ significantly from randomness (i.e., where there  
21      is statistical evidence of directionality). One-sample test for the mean angle was  
22      performed to test whether the population mean angle is statistically different  
23      from the given angle. In all of our circular statistics, von Mises distribution was  
24      assumed and also verified. Circular statistics were performed using CircStat: A  
25      MATLAB Toolbox [33, 40]. Please see detailed description of circular statistics  
26      in Supplementary Figure S3 and S5. Experiments were done in three biological  
27      replicates unless otherwise specified in Figure captions.

39  
40        **3. Results**  
41  
42

43        The adequate number of PODS®-hBDNF crystals to induce an effective neu-  
44      rotrophin gradient for otic neuronal differentiation and neurite outgrowth was  
45      determined by a three-dimensional FEA that predicts continuous concentra-  
46      tions of BDNF formed by the gradual release of BDNF from PODS®-hBDNF.  
47      We first empirically tested two available microchannel length—(i.e., Xona™ -  
48      XC150 [ $150\text{ }\mu\text{m}$ ] and Xona™ -XC450 [ $450\text{ }\mu\text{m}$ ]). This was done first because  
49      mass (i.e., BDNF) transport from the neurotrophin compartment through the  
50      micro-groove channels into the somal compartment is an important factor in  
51      generating the concentration gradient *via* diffusion mixing. We determined that  
52  
53  
54  
55  
56  
57  
58  
59  
60  
61  
62  
63  
64  
65

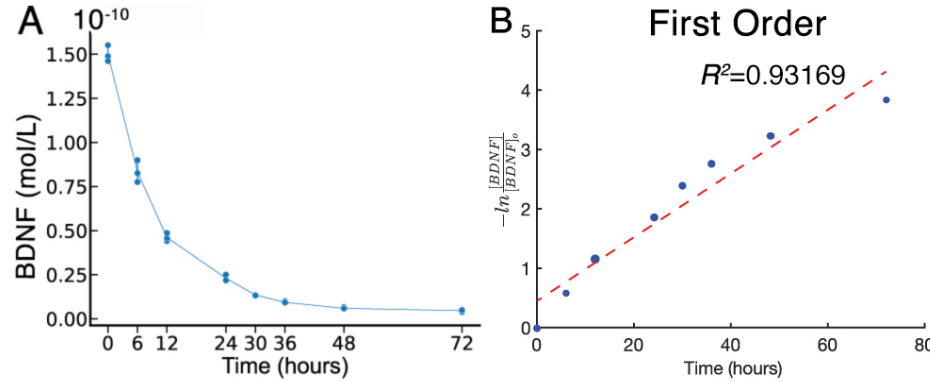


Figure 4: Chemical kinetics of Brain Derived Neurotrophic Factor (BDNF). (A): Concentration of recombinant hBDNF in solution over 72 hours after initial application. (B):  $\frac{1}{[BDNF]}$  data fit to first order curve. Please see other curve fit data in Supplemental Figure 1. Red line: fitted line, blue dots: individual data point.  $k_2$  is defined as slope of fitted curve.

the Xona<sup>TM</sup> Microfluidics XC450 was appropriate for this study as the XC-150's micro-groove channels were not long enough to generate an adequate concentration gradient throughout the somal compartment. This feature is relevant to human inner ear because the presence of the osseous spiral lamina and modiolus between the scala tympani and SGNs simulates the micro-groove channels in the Xona device [41, 42]. To mathmatically predict the BDNF concentration gradient formed by the gradual release of BDNF from PODS®-hBDNF, we next generated a three-dimensional geometry mesh of the Xona<sup>TM</sup> Microfluidics XC450 for FEA (Figure 3B(d)). Please also see Supplementary Figure S6 for detailed measurements of this 3-D dimensional mesh.

We next studied the chemical kinetics of the release and degradation of PODS®-hBDNF determined through the ELISA test (Figure 4) to establish the parameters for the FEA.

Degradation data were collected by monitoring hBDNF concentration over time after placing a predefined amount of PODS®-hBDNF into a single well of solution. Degradation data obtained for the first 72 hours indicate an exponential decay, suggesting first order kinetics (Figure 4). To confirm this notion,

we then performed a linear and nonlinear least square analysis of kinetic data obtained from ELISA by using MATLAB Curve Fitting Toolbox. We found that the corresponding  $R^2$  was 0.93169 for the first order curve-fit, confirming that the degradation kinetics was indeed first order (See also detail in Supplementary Figure S7). Here, two consecutive reactions occur: 1) the degradation and release of hBDNF from PODS® crystals, and 2) the degradation of hBDNF toward the degradation product (Equation (1)).



where  $DP$  is the degradation product of the released hBDNF, and  $k_1$  and  $k_2$  are the rate constants ( $\frac{1}{hour}$ ). The changing concentration of hBDNF (the intermediate product) can be expressed as follows:

$$C_{hBDNF} = C_{PODS} \cdot k_1 \cdot \left( \frac{e^{-k_1 \cdot t}}{k_2 - k_1} + \frac{e^{-k_2 \cdot t}}{k_1 - k_2} \right) \quad (2)$$

where  $C_{hBDNF}$  is the concentration of hBDNF and  $C_{PODS}$  is the concentration of PODS® [43].

The rate constant  $k_2 = 0.0679$  ( $\frac{1}{hour}$ ) was calculated by fitting data (obtained through an experiment monitoring recombinant hBDNF degradation) to a first-order reaction curve to identify the best fit.  $k_2$  was then plugged into Equation (2) solving for the concentration of the intermediate product of two consecutive first-order reactions to determine  $k_1$ , which was 0.00686 ( $\frac{1}{hour}$ ). PODS®-hBDNF release/degradation data are then curve fitted to this equation to approximate  $k_1$ . The resulting chemical gradient can be solved using Fick's second Law of diffusion by applying the appropriate boundary and initial conditions as follow:

$$\frac{\partial C}{\partial t} = \nabla \cdot (\nabla C \cdot D) - k_2 \cdot C \quad (3)$$

Boundary conditions:

$$\delta C \Big|_{walls} = 0 \quad (4)$$

and

339

$$\delta C \Big|_{PODS} = k_1 \cdot PODS_0 \cdot e^{-k_1 \cdot t} \quad (5)$$

Initial conditions:

$$C \Big|_{t=0} = 0 \quad (6)$$

where  $C$  is the concentration of hBDNF,  $D$  is diffusivity of hBDNF ( $6.76 \frac{mm^2}{day}$  [44]),  $-k_2 \cdot C$  is the sink term corresponding to the degradation and cell-utilization of the hBDNF.  $PODS_0$  is the initial concentration of the cargo protein (i.e., BDNF) within the PODS® crystals. The first boundary condition (Equation 4) shows that the concentrations of hBDNF at the walls of the microfluidic device are fixed at 0. The second boundary condition (Equation 5) represents the exponential nature of decay of the PODS®. Note that both of them are Neumann boundary conditions.

As mentioned, we used the first-order fitted data from our ELISA experiment and then determined the values of the  $k_{1,2}$  coefficients, which were then applied to the diffusion equation. The finite element model was then computed for different PODS®-hBDNF concentrations and time intervals to optimize the hBDNF concentration gradient for hPSC-derived ONP differentiation into SGNs and directed neurite extension. Figure 5 shows FEA-computed hBDNF concentration gradient for 20,000 PODS®-hBDNF from Day 1–7. Note that the BDNF concentrations were greater on D2–5 to promote neuronal differentiation and neurite outgrowth observed on D7 (Figure 5B). Computed diffusion flux was uniform throughout D1–7 (Figure 5C). Also note that highest concentration of hBDNF released from PODS®-crystals was greater than 50 pg/mL, the concentration sufficient for otic neuronal differentiation and neurite outgrowth of hPSC-derived ONP 3D spheroids from our previously published data [9]. For the optimization process in determining the adequate number of PODS®-hBDNF, we also performed FEA with 10,000 and 40,000 PODS®-hBDNF. Please see detailed discussion of how we determined the optimum concentration of 20,000 PODS®-hBDNF in Supplementary Figure S8.

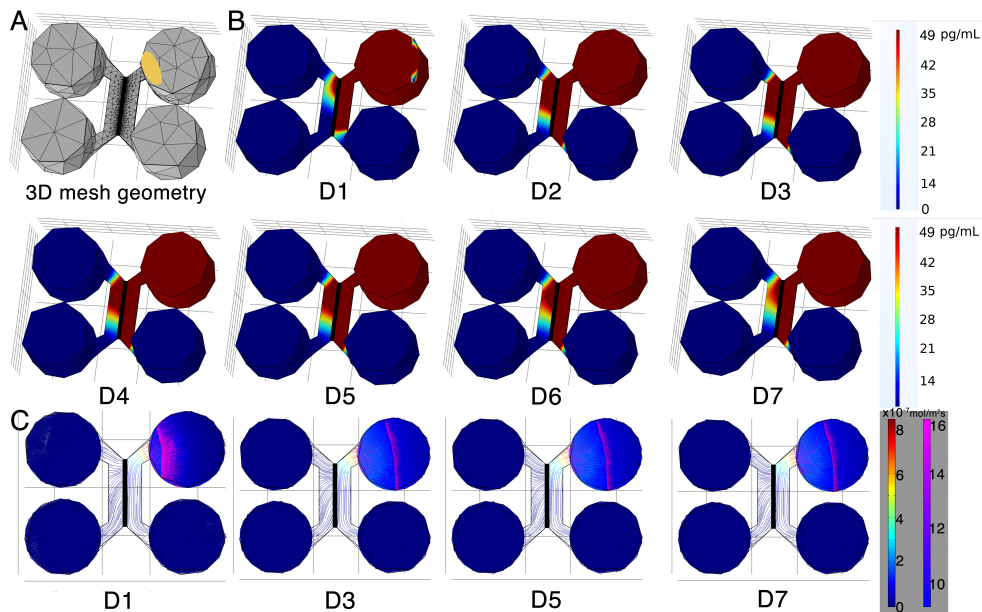


Figure 5: (A): 3D mesh geometry of a Xona<sup>TM</sup> XC450 created with Autodesk Inventor. An ellipse-shaped PODS<sup>®</sup>-hBDNF disc is shown in yellow. (B): Human BDNF concentration gradient for 20,000 PODS<sup>®</sup>-hBDNF from D1–D7. Note that the model does not account for media changes during the culture period. The corresponding color map is shown a range from 0 ng/mL to 49 ng/mL. (C): Diffusion flux ( $\text{mol}/\text{m}^2\text{s}$ ) was computed using COMSOL Chemical Engineering module on D1, D3, D5, and D7.

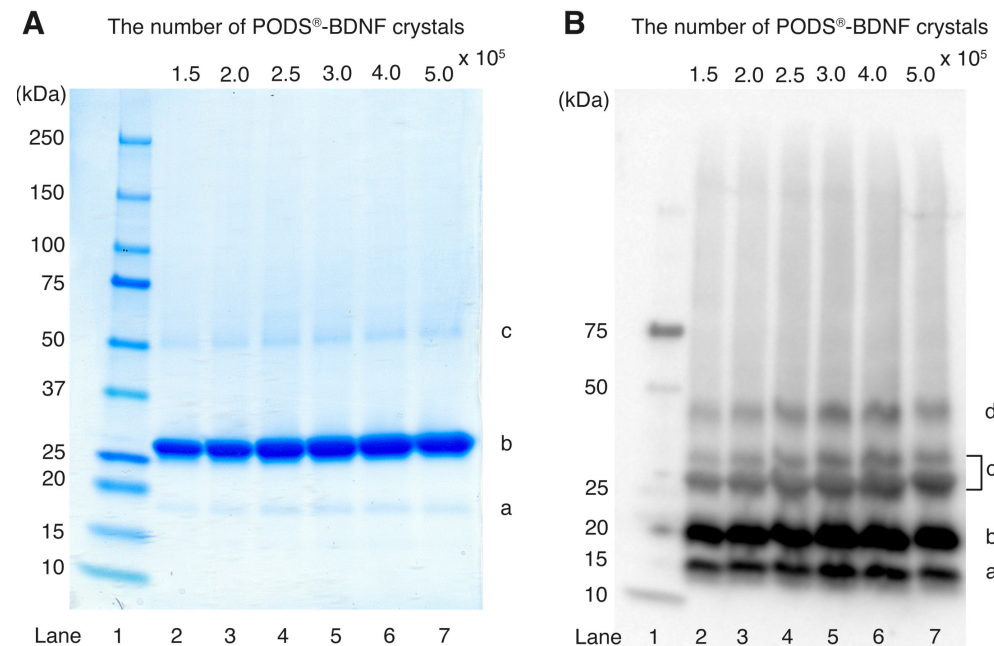


Figure 6: (A): SDS-PAGE analysis of PODS®-hBDNF. Samples containing six quantities of PODS®-hBDNF crystals were run on precast 4-15% polyacrylamide mini-gels and stained with Coomassie G-250 solution for visualization. Protein bands appear at approximately 18.8 (a), 28.0 (b), and 46.8 kDa (c). Lane 1: molecular weight marker. Lanes 2-7: samples containing

1  
2  
3  
4  
5  
6  
7  
8  
9        SDS-PAGE was used to separate PODS<sup>®</sup>-hBDNF crystals into its con-  
10      stituent proteins to determine the molar ratio of polyhedrin to BDNF. Visualiza-  
11      tion with Coomassie G-250 solution (Figure 6A) revealed three distinct protein  
12      bands at 18.8 (a), 28.0 (b), and 46.8 (c) kDa, which correspond with the molec-  
13      ular weights of H1-tagged BDNF monomer, polyhedrin, and H1-tagged BDNF  
14      monomer attached with polyhedrin, respectively. Western blot analysis was sub-  
15      sequently conducted to confirm the identity of the 18.8 kDa band as hBDNF.  
16  
17      Enhanced chemiluminescence (Figure 6B) revealed four protein bands at 14.0  
18      (a), 18.8 (b), 37.6 (c), and 46.8 (d) kDa, which correspond with the molecular  
19      weights of hBDNF monomer, H1-tagged BDNF monomer, H1-tagged BDNF  
20      dimer, and H1-tagged BDNF monomer attached with polyhedrin. Immunoblot  
21      detection of the 18.8 kDa band further implicates its identity as hBDNF. SDS-  
22      PAGE images were converted to 8-bit grayscale and mean corrected integrated  
23      378 pixel intensity values were calculated for protein bands located at 28.0 and 18.8  
24      379 kDa; the protein band detected at 46.8 kDa was omitted from the final com-  
25      380 putation based on the notion that it contained a 1:1 ratio of polyhedrin to  
26      381 BDNF. Results indicate that the molecular ratio of polyhedrin to hBDNF is  
27      382 approximately 17:1.

28  
29        To objectively compare the degree of otic neuronal differentiation in hPSC-  
30      derived ONPs, we performed quantitative analysis of PAX8 and GATA3 double-  
31      384 positive cells using immunocytochemistry. We chose PAX8 and GATA3 for this  
32      385 analysis because our previous studies indicated high expression of these protein  
33      386 markers in late-stage ONPs and early-stage SGNs [8, 9, 24]. Cells were stained  
34      387 in the somal compartment of the Xona<sup>TM</sup> device, highlighted in green in Figure  
35      388 7A. Figure 7B shows the resulting image of cells in the somal compartment, and  
36      389 a heat-map representation of the percentage of double-positive cells is shown  
37      390 in Figure 7C. It should be noted here that the heatmap is sensitive to the  
38      391 differences in cell density across channel. This was accounted by averaging  
39      392 the double-positivity across three biological replicates. The heat-map indicates  
40      393 higher double-positivity in the upper region of the somal compartment, which  
41      394 is closest to the PODS<sup>®</sup>-hBDNF disc placement (shown in a orange ellipse in  
42      395 Figure 7D).

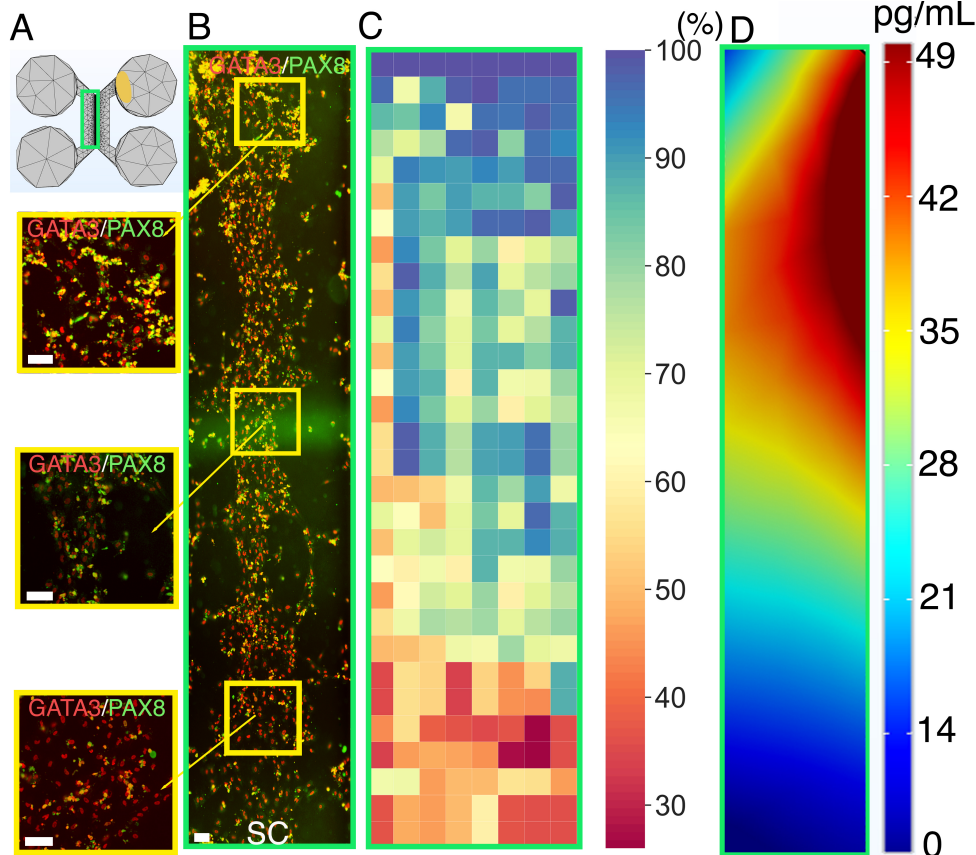


Figure 7: Human PSC-derived late-stage ONPs grown in a microfluidic device at Day 7 were stained for GATA3 (red) and PAX8 (green). (A): Geometry mesh of the microfluidic device Xona<sup>TM</sup> XC450 generated by Autodesk Inventor. The green square indicates the cell seeding location in the somal compartment of the device. An ellipse-shaped PODS<sup>®</sup>-hBDNF disc is shown in yellow. (B): Cells were analyzed by staining with neuronal markers GATA3 (red) and PAX8 (green). Yellow highlighted regions are magnified on the left. SC: somal compartment. (C): Heat-map representation of double-positivity of hPSC-derived ONPs in the device for GATA3 and PAX8 ( $n = 3$ ). Double-positivity increases from the lower to the upper portion of the somal compartment, suggesting that the higher BDNF concentration in the upper portion of the device improves differentiation. Scale bar: 100  $\mu\text{m}$ . (D): Prediction of BDNF concentration gradient released from PODS<sup>®</sup>-hBDNF at seven days in culture using a finite element model. The corresponding color map is shown with a range from 0–49 pg/mL.

1  
2  
3  
4  
5  
6  
7  
8  
9       396 Figure 7A) in the neurotrophin compartment. Double-positivity decreases in  
10      397 the somal compartment as distance from the PODS®-hBDNF disk increases,  
11      398 supporting the presence of a BDNF neurotrophin gradient as predicted by our  
12      399 computational model calculation (Figure 7D).

13  
14  
15       400 We defined two hypothetical directional angles to predict the orientation of  
16      401 hPSC-derived ONPs and neurite growth (Figure 8). The  $n$ -dimensional Eu-  
17      402 clidean space, denoted by  $\mathbb{R}^n$ , is a linear vector space in that we can use polar  
18      403 coordinates to compute the directionality of cells and neurites [45]. Here, we  
19      404 used  $n = 1$  and  $2$ . For one-dimensional Euclidean space ( $n = 1$ ), we simply drew  
20      405 a line for the Euclidean distance—the shortest distance between two points as  
21      406 shown in Figure 8A(b) (dark green lines). The two points were 1) the center  
22      407 point of a PODS®-hBDNF disk ( $P$ ) and 2) the mid point of the medial side  
23      408 (i.e., the near side to microgroove channels) of a pre-designated square  
24      409 (shown as a black square, zone 1–5 in Figure 8), respectively. The Euclidean  
25      410 distance angle (EDA),  $\phi_i$ , was defined as the angle between the horizontal line  
26      411 zero direction and the line  $PQ_i$  that consists of the Euclidean distance where  $i$   
27      412 = 1–5.

28  
29  
30       413 For two-dimensional Euclidean space ( $n = 2$ ), we utilized Fick's first law,  
31      414 which dictates that the diffusion flux ( $D$ ) is proportional to the concentration  
32      415 gradient ( $C$ ) [46]. Based on this theorem, the direction of a flow vector can  
33      416 be used to represent concentration gradient for the directionality. We hypothe-  
34      417 sized here that cell orientation is directionally controlled by the flux vector  
35      418 which is driven by the concentration gradient. Figure 8B shows the flow vectors  
36      419 in a somal compartment at Day 7 computed by COMSOL Chemical engineering  
37      420 module. We averaged the 10 flow vectors in each of five zones in Figure 8 to  
38      421 compute diffusion flux angle (DFA),  $\psi_i$ , where  $i = 1–5$  in Figure 8. To lighten  
39      422 the computational intensity, we reduced a dimension from 3D to 2D to com-  
40      423 pute diffusion Flux. Please see justification in Supplementary Data. All of the  
41      424 computed EDAs and DFAs can be found in Supplementary Table 2.

42  
43  
44       425 Figure 9 shows time-series of microscopic phase-contrast photomicrographs  
45      426 obtained on Day 1, 3, and 7 in the five zones in a Xona™ XC450. Each pre-

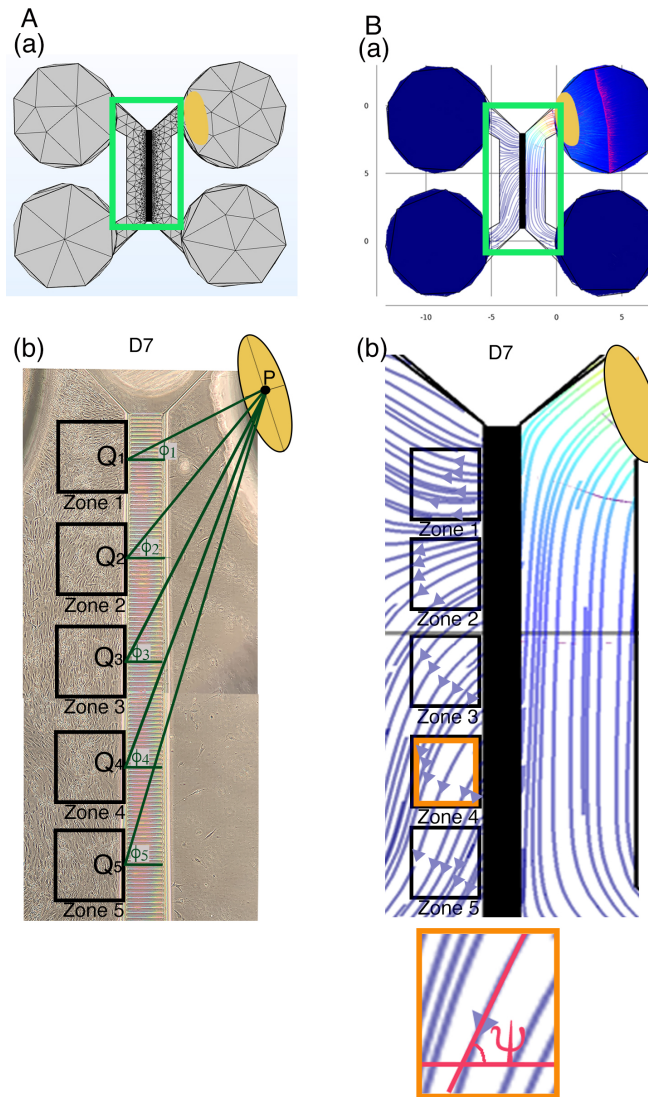
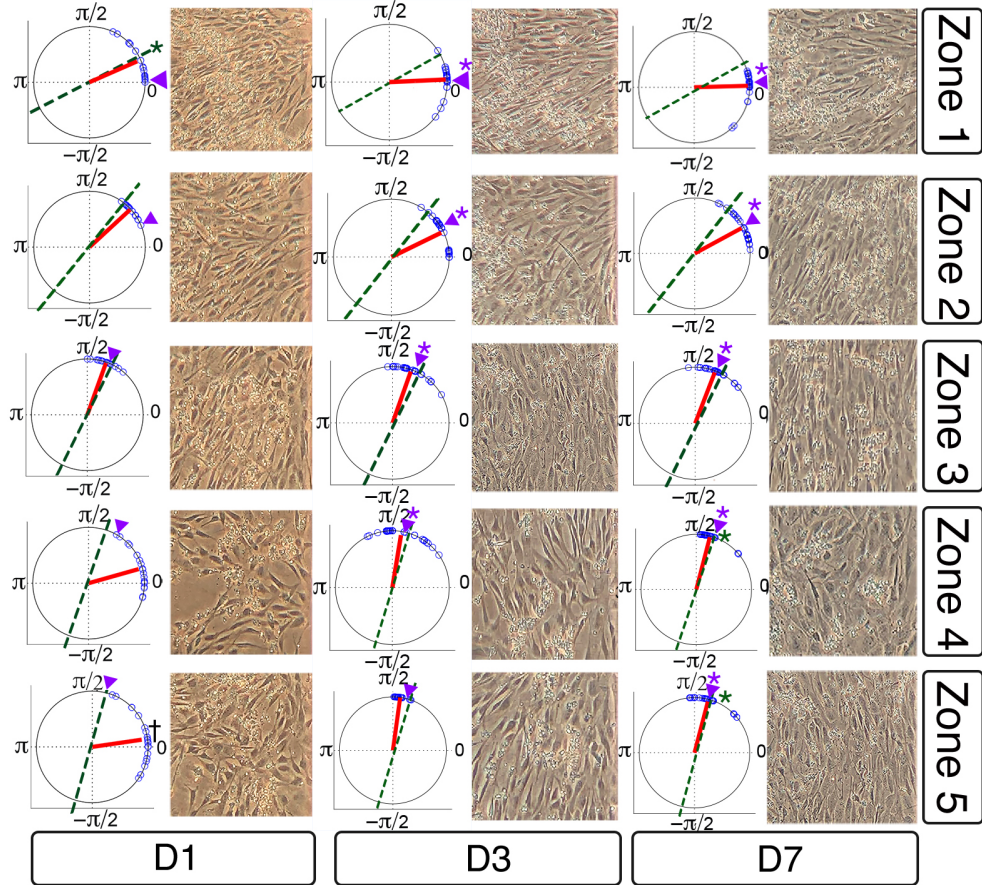


Figure 8: (A): Defining the Euclidean distance angle (EDA). (a) X-Y plane geometry mesh of a Xona™ XC450 device. Green square shows an area corresponding to a phase-contrast image below. An ellipse-shaped PODS®-hBDNF disc is shown in yellow. (b) hPSC-derived ONPs were cultured in a Xona™ XC450 for seven days (D7). Yellow ellipse once again indicates the location of a disk contains PODS®-hBDNF crystals (P: the center of this ellipse). In the somal compartment of the Xona™ XC450 device, we defined Zone 1–5, shown in black square. A line was drawn from the center of the PODS®-hBDNF disk (P) to (Q<sub>1–5</sub>) (i.e., the near side to microgroove channels) of a pre-designated square (shown as a black square, zone 1–5) [i.e.,zone 1–5]. The Euclidean distance angle (EDA) for zone 1–5 was defined as  $\phi_i$ ,  $i = 1–5$ . (B): Defining diffusion flux angle (DFA). (a) Diffusion flux in a Xona™ XC450. Green squared area show a somal and neurotrophin compartment, which are magnified in (b). (b) Magnified image of diffusion flux of Zone 1–5 in a Xona™ XC450. Orange highlighted zone (zone 4) was magnified at the bottom of (b), defining a DFA ( $\psi$ ).



45  
46  
47  
48  
49  
50  
51  
52  
53  
54  
55  
56  
57  
58  
59  
60  
61  
62  
63  
64  
65

Figure 9: Preferred cell orientation analysis. Sequential phase-contrast images of a somal compartment of a Xona™ XC450 device in zone 1–5 (see Figure 8) on day 1 (D1), day 3 (D3), and day 7 (D7). A corresponding polar histogram indicates preferred orientation of hPSC-derived ONPs in an angle ( $0$ – $2\pi$  radians) in blue circles. Mean vector angle is shown in red line. Green dotted line shows Euclidean Distance Angle (EDA) and purple triangle indicates Diffusion Flow Angle (DFA). † symbol indicates that  $p$  value  $> 0.01$ . \* symbol indicates that the mean vector angle fits within the 95% confidence internal ( $\alpha < 0.05$ ).

ferred orientation of any given cell was computed and then plotted on a polar diagram (blue circle). Mean vector angle (MVA, shown in red line on Figure 9) and median vector angle were computed. All of the polar diagrams in Figure 9 show that preferred orientation of hPSC-derived ONPs distribute in an unimodal distribution. We also confirmed that a von Mises distribution is appropriate for these sets of data (See Supplementary Figure S9). We, therefore, then tested further to see if the cells had tendency to be oriented to a certain direction. To test this hypothesis, we used the Rayleigh test of uniformity to evaluate whether there is statistical evidence of circular directionality [32]. Computed  $p$  values for all the 15 conditions were less than 0.05, demonstrating that all of the conditions had statistically significant directionality. To further validate whether the observed angles have a tendency to cluster around the two hypothetical angles (i.e., EDA and DFA), we then performed the V test. Once again,  $p$  values for all 15 conditions were less than 0.05 except one (Zone 5 on Day 1), re-demonstrating that most of the conditions had statistically significant tendencies to cluster around the EDAs and DFAs. Finally, to investigate whether the preferred orientation of the cells were clustered around the EDAs or DFAs, we performed one sample test for the mean vector angle, which is similar to a one sample t-test on a linear scale. There was only one condition (Zone 1, day 1) that was statistically significant for EDA, whereas most of the conditions on Day 3 and 7 were statistically significant for DFA. Therefore, our results here demonstrated that hPSC-derived ONPs had greater tendency to cluster around DFA than EDA. All computed statistical values are shown in Supplementary Table S2.

To evaluate the direction of neurites of hPSC-derived ONPs, we first defined EDA in Region 1-3 ( $\phi'_j$ ,  $j = 1 - 3$ ) (Figure 10A) and DFA ( $\psi'_j$ ,  $j = 1 - 3$ ); similarly defined  $\phi_i$  and  $\psi_i$  as in Figure 8. All of the EDAs and DFAs defined here can be found in Supplementary Table S3. Polar histograms of the neurite direction angle in Region 1-3 indicated that the two longest neurites were bimodal in nature (Figure 10B). In contrast, polar histograms of those cultured with rhBDNF (negative control) and 800,000 PODS<sup>®</sup>-BNDF (positive control)

1  
2  
3  
4  
5  
6  
7  
8  
9  
10  
11  
12  
13  
14  
15  
16  
17  
18  
19  
20  
21  
22  
23  
24  
25  
26  
27  
28  
29  
30  
31  
32  
33  
34  
35  
36  
37  
38  
39  
40  
41  
42  
43  
44  
45  
46  
47  
48  
49  
50  
51  
52  
53  
54  
55  
56  
57  
58  
59  
60  
61  
62  
63  
64  
65

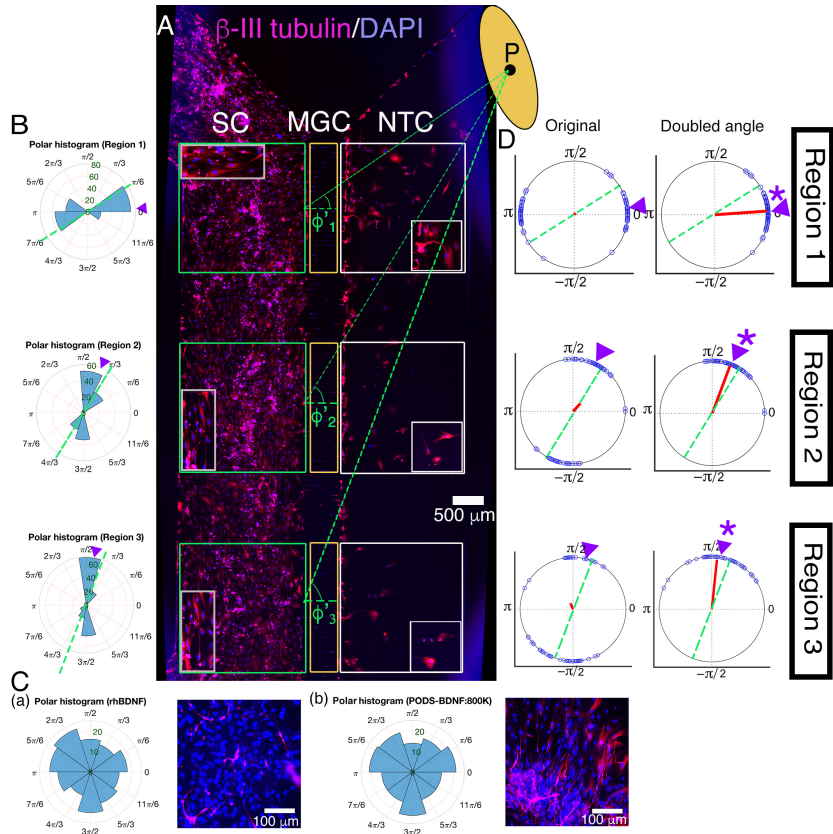


Figure 10: (A): Immunohistochemistry of hPSC-derived ONPs cultured in the Xona<sup>TM</sup> XC450 for seven days with  $\beta$ -III-Tubulin (pink fluorescence) and DAPI (blue fluorescence). A green line was drawn from the center of the BDNF disk (P) to the mid point of each of three pre-determined squares (Region 1–3) in the somal compartment to define Euclidean Distance Angle (EDA:  $\phi_i^c$ ,  $i = 1 - 3$ ). Green square: somal compartment (SC); yellow square: microgroove channels (MGC); White square: Neurotrophin compartment (NTC). High-power magnified images of the NTC and SC are shown. An ellipse-shaped PODS®-hBDNF disc is shown in yellow. P: the center of the disk.(B): Polar histogram of neurite directional angles of hPSC-derived ONPs in the Xona<sup>TM</sup> XC450 at Day 7 (D7). The two longest neurites were measured. EDA: green dotted line. DFA: purple triangle. (C): (a) Right: Polar histogram of neurite directional angles of hPSC-derived ONPs cultured with 20 ng/mL of recombinant human BDNF for seven days. Left: Corresponding photomicrograph of immunocytochemistry with  $\beta$ -III tubulin (pink) and DAPI (blue). (b) Right: Polar histogram of neurite directional angles of hPSC-derived ONPs cultured with 800,000 of PODS®-hBDNF for seven days. Left: Corresponding photomicrograph of immunocytochemistry with  $\beta$ -III tubulin (pink) and DAPI (blue). (D): A circular plot of neurite directional angle of hPSC-derived ONPs in Region 1–3. Once again, the two longest neurites were plotted on a unit circle. Right column: Original directional angle distribution. Left column: the method of doubling the angle applied to the original data. Each datum point is shown as a blue circle. Mean vector angle is shown as a red line. Green dotted line shows Euclidean Distance Angle (EDA) and purple triangle indicates Diffusion Flow Angle (DFA). \* symbol indicates that the mean vector angle fits within the 95% confidence internal ( $\alpha < 0.05$ ).

1  
2  
3  
4  
5  
6  
7  
8  
9       458 did not indicate bimodal distribution—the neurites did not show directionality  
10      459 (Figure 10C). The Rayleigh test of uniformity for both the positive and negative  
11      460 control were greater than 0.05, demonstrating that both of the conditions had  
12      461 no statistically significant directionality (Supplementary Table S3: highlighted  
13      462 in green). We also analyzed the direction of the neurites using circular statistics.  
14      463 To obtain more realistic mean vector angles, we doubled each angle and reduced  
15      464 the multiples modulo 360°. In circular statistics, the bimodal distributed data  
16      465 can be transformed into a unimodal data by doubling the angle [32]. The mean  
17      466 vector angles in Figure 10D (right column) indicates the situation where the  
18      467 vectors were canceled out between the two groups of angles distributed in a bi-  
19      468 modal fashion, resulting in inaccurate representation. A circular plot in Figure  
20      469 10D (right column) showed doubled angles, representing actual representation  
21      470 of the neurite vector angles. In all of the three regions, the Reyleigh test and V  
22      471 test for EDA and DFA indicated directionality (Supplementary Table S3). One  
23      472 sample test for the mean vector angles in Region 1–3 indicated that they were  
24      473 not statistically different from DFA, but all of the three mean vector angles were  
25      474 statistically different from EDA.

35  
36       475 We also stained the devices for  $\beta$ -III tubulin to track neurite growth and  
37      476 extension across the micro-groove channels as well as cell migration in three  
38      477 selected regions (Figure 10A). The location of the PODS®-hBDNF disk in re-  
39      478 lation to the regions of interest in Figure 11A is indicated by a yellow circle.  
40      479 Quantitative analyses were performed and summarized in Figure 11B. Our data  
41      480 indicate that neurite length is dependent on BDNF concentration, with greater  
42      481 amounts of PODS®-hBDNF promoting longer neurite growth (Figure 11B(a)).  
43      482 Lesser amounts of PODS®-hBDNF, however, are necessary to create an ap-  
44      483 propriate concentration gradient. In the presence of 20,000 PODS®-hBDNF,  
45      484 both neurite extension into the microchannels and cell migration into the neu-  
46      485 rotrophin compartment are greatest in the region closest to the BDNF source  
47      486 and decrease further from the PODS®-hBDNF (Figure 11B(b,c)). Cell migra-  
48      487 tion is dependent on the distance from the source of BDNF, thus suggesting the  
49      488 presence of a BDNF gradient as predicted by our model. Note that the Xona

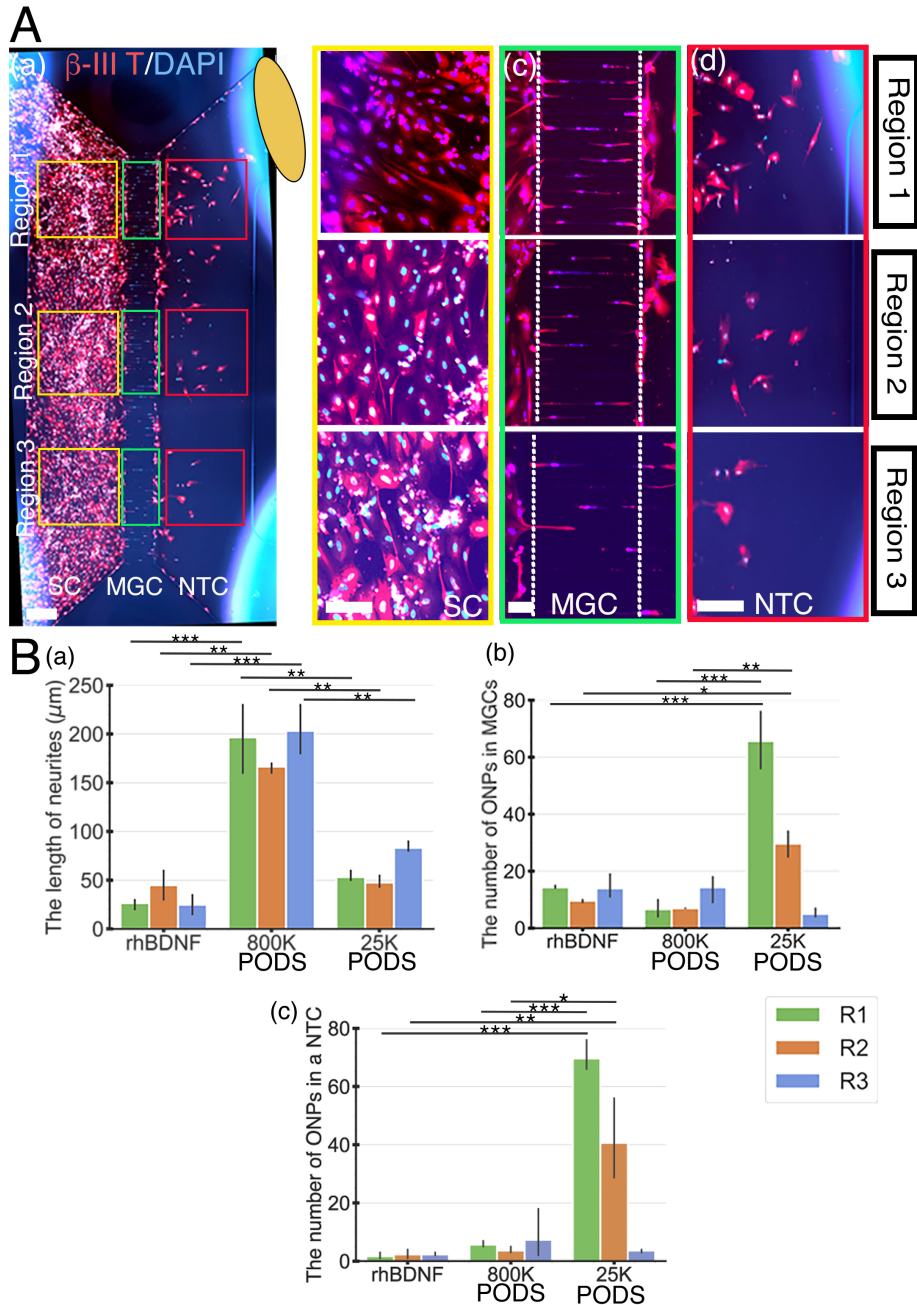


Figure 11: Human PSC-derived late-stage ONPs in the microfluidic device were stained with  $\beta$ -III tubulin (red) and DAPI (blue) to measure cell migration. (A): Late-stage ONPs stained after seven days in culture (a) with regions highlighted and magnified in the somal compartment (b), microgroove channels (c), and neurotrophin compartment (d). SC: somal compartment, MGC: microgroove channels, NTC: neurotrophic compartment. An ellipse-shaped PODS<sup>®</sup>-hBDNF disc is shown in yellow. Scale bar (a): 500  $\mu\text{m}$ ; (b)–(d): 100  $\mu\text{m}$ . (B): Quantitative analyses of cell migration and neurite extension in devices using recombinant human BDNF, 800,000 PODS<sup>®</sup>-hBDNF, or 20,000 PODS<sup>®</sup>-hBDNF. \* :  $p < 0.05$ , \*\*:  $p < 0.01$ , \*\*\*:  $p < 0.001$ .

1  
2  
3  
4  
5  
6  
7  
8  
9     489 microchannels intended to prevent from migration across channels.  
10  
11

12     490 **4. Discussion**  
13  
14

15     491 *4.1. Challenges in neurotrophin treatment in the inner ear*  
16  
17

18     492 This is a proof-of-concept study for the realization of a neurotrophic strip  
19     493 to ascertain its scientific/technological parameters in a controlled *in vitro* en-  
20     494 vironment. Neurotrophin gradients have been studied for in multiple contexts  
21     495 [47, 48, 49]. However, it has not been feasible to reliably provide such a gradient  
22     496 to neurons neither *in vitro* nor *in vivo*, primarily because of technical challenges.  
23  
24     497 While neurotrophin treatment has been recognized as a potential treatment for  
25     498 sensorineural hearing loss, there has not been clinical success in this avenue to  
26     499 date. Most recent relevant clinical trials used adeno-associated virus (AAV2)  
27     500 to deliver BDNF to the brain [50]. Although exciting, this treatment does not  
28     501 attempt to control the concentration of BDNF, which could potentially inter-  
29     502 fere with normal functions in a target organ [51]. Furthermore, this treatment  
30     503 may not be applicable to the inner ear. In this study, we used PODS®-hBDNF  
31     504 to provide a neurotrophic gradient in a controlled fashion. Our result indi-  
32     505 cated 20,000 PODS-BDNF allowed for hBDNF neurotrophin gradient such that  
33     506 hESC-derived ONPs survived, differentiated toward human SGNs, and also es-  
34     507 tablished directional neurite outgrowth in a microfluidic device.  
35  
36  
37  
38  
39  
40  
41  
42  
43

44     508 *4.2. Microfluidic device-generated gradient*  
45  
46

47     509 We used a microfluidic device to advance our understanding of directional  
48     510 neurite growth and otic neuronal differentiation in response to a BDNF concen-  
49     511 tration gradient [52]. Among many *in vitro* concentration gradient sustaining  
50     512 culture devices, microfluidic devices have overcome many of the deficits that  
51     513 conventional platforms (i.e., the Boyden chamber, Dunn chambers, or compart-  
52     514 mentalized diffusion chambers) face [52]. Conventional platforms tend to be  
53     515 sub-optimal to manipulate small volumes of fluid at the order of microliters.  
54     516 Growth factors and proteins are used in minute amounts in our microfluidic  
55  
56  
57  
58  
59  
60  
61  
62  
63  
64  
65

1  
2  
3  
4  
5  
6  
7  
8  
9       517 device, and cultured stem cells are able to interact with endogenous factors. As  
10      518 mentioned earlier, this micro-environment more accurately represents *in vivo*  
11      519 conditions. The Xona<sup>TM</sup> device can be used to sustain a three-dimensional  
12      520 concentration gradient over time (duration dependent on the half-life of the  
13      521 molecule) due to its microchannel array. The device limits convective flow in  
14      522 the gradient-forming areas by introducing microgroove channels that generate  
15      523 high fluidic resistance, thereby limiting flow to diffusion. The high resistance  
16      524 of the microchannel array also prolongs diffusion across them, thereby increasing  
17      525 both gradient formation and gradient steepness. These features allowed us  
18      526 to generate a FEM, which predicted the necessary number of PODS®-BDNF  
19      527 crystals for a BDNF gradient. Note, however, that this environment is different  
20      528 from the micro environment in the inner ear. A mesh geometry of the cochlea  
21      529 will be needed to compute the PODS®-BDNF crystal number for our next step  
22      530 of this study.

31  
32       531 *4.3. BDNF and Polyhederin protein*

33  
34       532 Over the course of past 20–30 years, it has been established that BDNF me-  
35      533 diates survival and differentiation activities on SGNs by binding and activating  
36      534 the tyrosine kinase receptor kinase B (TrkB), a member of the larger family  
37      535 of Trk receptors [20]. Numerous studies have reported that BDNF can palliate  
38      536 SGN degeneration in ototoxically deafened animals, a widely accepted model for  
39      537 retrograde trans-synaptic SGN degeneration secondary to hair cell destruction  
40      538 [13, 14, 53, 54]. Additionally, it has been confirmed that there is a positive corre-  
41      539 lation between SGN counts and CI performance [55]. It is then safe to presume  
42      540 that treating CI recipients with BDNF would enhance overall CI performance,  
43      541 by preserving SGNs and their neurites. However, simply introducing recombi-  
44      542 nant hBDNF into the inner ear poses significant hurdles. Although promising,  
45      543 human BDNF treatment has not been currently implemented in the inner ear.  
46      544 Unsuccessful BDNF treatment can be explained by several factors [56].

47  
48       545 The blood half-life of BDNF protein is extremely short, only 1–10 min in  
49      546 the plasma [57, 58] and one hour in CSF [59]. The BDNF's high degrada-

1  
2  
3  
4  
5  
6  
7  
8  
9        547 tion rate would require continuous replenishment, impractical for clinical use.  
10      548 Furthermore, introduction of a homogeneous solution of BDNF would promote  
11      549 nondirectional neurite growth where directed neurite growth is essential for de-  
12      550 signing our new-generation bioactive CI, as depicted in Figure 1A. Directing  
13      551 neurite growth towards the CI electrode array is pivotal in the ultimate goal  
14      552 of enhancing performance through the narrowing of the electrode-neuron gap.  
15      553 The PODS® system precludes the phenomena by its localized, gradual release  
16      554 of growth factor. The steady supply of BDNF from a localized origin not only  
17      555 creates a concentration gradient, but maintains it over time. As seen in Figures  
18      556 4–6, we were able to perform a finite element analysis based on data we collected  
19      557 describing the chemical release kinetics and molar ratio of PODS®-BDNF sys-  
20      558 tem. It is clearly visible that the slow-release nature of PODS®-BDNF results  
21      559 in a concentration gradient over the course of Day 1–7 (Figure 5).

22  
23        560 It should be noted that our FEM assumes free diffusion of the hBDNF  
24      561 protein. In biological cell-culture conditions, BDNF released from PODS®-  
25      562 BDNF has tendency to adhere to the walls of the culture device because BDNF  
26      563 is a “sticky” protein of about 27 kDa (mature BDNF dimer) and it is positively  
27      564 charged under physiological conditions (isoelectric point, pI = 9.4) [60]. As such,  
28      565 the physio-chemical properties of BDNF have made the recombinant protein  
29      566 difficult to diffuse. This phenomenon was observable in preliminary data where  
30      567 the ONPs failed to survive past 1–3 days of culture (data not shown). To  
31      568 circumvent this issue we infused the culture media with a carrier protein (i.e.,  
32      569 BSA), hypothesizing that the albumin would act as a carrier for the released  
33      570 BDNF and allow for free diffusion throughout the microfluidic device [61]. This  
34      571 hypothesis is supported by our sets of biological verification data (Figures 7–11)  
35      572 that clearly shows that hPSC-derived ONPs responded to the modification by  
36      573 exhibiting the expected cell body orientation, unidirectional neurite extension,  
37      574 and neurite length. Note that albumin is the single protein found in highest  
38      575 concentrations in the perilymph [62], therefore, a carrier protein will not be  
39      576 needed in our future *in vivo* study.

1  
2  
3  
4  
5  
6  
7  
8  
9       577 *4.4. Intracellular signaling initiated by Thyrosine kinase B receptor*

10  
11       578 Another issue we need to consider in interpretation of our results is the in-  
12       579 tracellular cell signaling mechanism elicited by hBDNF. Human BDNF (mature  
13       580 dimeric form) binds with high affinity to its TrkB receptor. The binding of  
14       581 BDNF to a TrkB receptor has proven to have significant importance for the  
15       582 proneuronal effects of BDNF [20]. Upon binding BDNF, TrkB dimerizes, and  
16       583 activates intrinsic kinase activities and other complex set of intracellular sig-  
17       584 naling cascades, which is beyond the scope of this study. However, it should  
18       585 be noted that activation of TrkB receptor by neurotrophin binding causes the  
19       586 TrkB protein to be internalized in endosomes on the cellular membrane [63].  
20       587 Endosomes can then be transported to the soma. Therefore, the proneuronal  
21       588 effects of hBDNF in our results might have highly depended on the status of  
22       589 TrkB receptors on the cell membrane of hPSC-derived ONPs. Our previous  
23       590 study has demonstrated that strong expression of a TrkB receptor on derived  
24       591 ONPs [24], however, more detailed studies on TrkB receptors on hPSC-derived  
25       592 ONP and SGNs will be needed.

34  
35       593 *4.5. Degradation of PODS® crystals by protease*

36  
37       594 In cell culture, degradation of PODS®-hBDNF is likely due to the activity  
38       595 of cell-secreted proteases. The proteases break down the peptide bonds of the  
39       596 encasing polyhedrin protein, creating openings in the structure to allow release  
40       597 of the hBDNF. Therefore, the presence of proteases is imperative for the proper  
41       598 utilization of the PODS® crystals. Additionally, these proteases are responsible  
42       599 for the degradation of the released BDNF. Because stem cells are not present  
43       600 in the culture media used for the PODS® degradation kinetics experiments, we  
44       601 infused the media with 10% FBS, which naturally contains proteases, to promote  
45       602 polyhedrin degradation, BDNF release, and BDNF degradation to attain results  
46       603 that more accurately describe *in vitro* events. Moreover, since the cells and  
47       604 PODS are initially segregated into separate compartments within the culture  
48       605 device, cell-secreted proteases are unlikely to reach and degrade the PODS in  
49       606 time to support ONP survival and differentiation. Infusion of FBS was therefore

1  
2  
3  
4  
5  
6  
7  
8  
9 required in these experiments as well. In clinical use, however, we presume  
10 that cell-secreted proteases will be readily present in the inner ear and would  
11 therefore preclude the need for artificial supplementation.  
12

13  
14 610 *4.6. A concept design: Neurotrophic strip*  
15

16 611 The plateau in CI performance in treatment of sensorineural hearing loss has  
17 driven researchers to develop innovative supplementary treatment strategies to  
18 push the field past this hurdle. Our approach strives to directly address the  
19 issue at its core: the electrode-neuron gap, which can lead to serious implica-  
20 tions include low spatial frequency resolution and high power consumption. We  
21 can use our data as a launchpad for the neurotrophic strip (NS). The NS is a  
22 biointerface concept that integrates an extended-release source of growth factor  
23 to facilitate a protein gradient. Implanted in conjunction with the CI, it acts  
24 as a bridge between the extant SGNs and implanted late-ONPs grown on the  
25 electrode itself. The NS would promote survival of both cell populations, dif-  
26 ferentiation of the late ONP implants, promote directional neurite growth and  
27 synaptogenesis between the two, effectively creating a neuronal network between  
28 the patient and the implanted CI. Each electrode would be able to stimulate cell  
29 bodies at exceptionally high resolution, essential for greater intonation differ-  
30 entiability (required for effective social interaction and music appreciation) and  
31 so, increased quality of life for millions. Our successful outcomes are essential  
32 to make a neurotrophic strip feasible in *in vivo* environment.  
33

34 628 *4.7. The limitations of this study and future direction*  
35

36 629 There are some limitations associated with this study. First, the reduction of  
37 spacial dimension to 2D for diffusion modeling certainly affected the flux vector,  
38 which determines the predicted concentration vector. Given that the thickness  
39 (i.e., Z-axis) of the microfluidic device was 100  $\mu\text{m}$ , we estimated that the effect  
40 was minimal. In the future, we plan to use PSC-derived 3D spheroids in a somal  
41 compartment so that flux vector and concentration gradient vector can more  
42 accurately model the cell behavior. In this way, we will be able to circumvent  
43

1  
2  
3  
4  
5  
6  
7  
8  
9       636 the need to reduce diffusion calculations to 2D for computation performance in  
10      637 the modeling.

12       638 Secondly, we required to generate a model in that the BDNF's biological  
13      639 transportation phenomenon from a PODS®-hBDNF disk to a somal compart-  
14      640 ment of a Xona™ device. Note that in this model, we focused on the major  
15      641 dependent variable, BDNF concentration gradient to model the biological phe-  
16      642 nomenon. Other physical variables to promote cell migration, otic neuronal  
17      643 differentiation, and neurite growth were not take into consideration. These  
18      644 variables include electotaxis (electrical potential), durotaxis (matrix's stiffness  
19      645 [i.e., laminin 511 in our case]) [64], mechanotaxis (cell strain), and lastly cell  
20      646 migration by random walk [65]. In our future study, we will take these vari-  
21      647 ables into consideration to more accurately represent the migration and neurite  
22      648 growth of hPSC-derived ONPs.

23       649 Insufficient contrast between cells and background in phase contrast images  
24      650 led to inaccuracies in cell orientation computation for some images. To address  
25      651 this issue, poor quality images were disregarded in the quantitative analysis.  
26      652 We occasionally used manual measurement for accuracy. Our future study may  
27      653 entail automated time-series cell analysis, which would allow more accurate  
28      654 measurement. Also, another way to address this issue would be with a cell  
29      655 membrane staining in the future.

30       656 While 20,000 of PODS®-hBDNF were necessary for hPSC-derived ONPs for  
31      657 otic neuronal differentiation and directional neurite outgrowth, this condition  
32      658 may not be sufficient. For instance, it is still not known whether the effects  
33      659 of other neurotrophic factors such as Neurotrophin-3 and Glial cell line-derived  
34      660 neurotrophic factor could have a positive effect on ONP growth [20, 66, 67]. We  
35      661 are planning to investigate these neurotrophic factors in the future. Other fac-  
36      662 tors that could have an impact on directional neurite growth include endogenous  
37      663 factors secreted from hPSC-derived ONPs. While our previous study demon-  
38      664 strated that hPSC-derived ONPs only secreted negligible amount of BDNF that  
39      665 were detected by ELISA [9], currently we do not have any data on other neu-  
40      666 rotrophic factors or other molecules that could have affected directional neurite

1  
2  
3  
4  
5  
6  
7  
8  
9       667 growth in the inner ear. We chose BDNF first to study because the most inten-  
10      668 sively studied neurotrophic factor in the field of hearing research is BDNF [20].  
11  
12      669 Previous studies have indicated that neurotrophic supports of SGNs are mainly  
13      670 from BDNF and neurotrophin-3 (NT-3) [20, 60]. Therefore, the potential con-  
14      671 founding effect of the secretions of other neurotrophic factors and molecules  
15      672 secreted from derived SGNs are likely NT-3, for which further investigation is  
16      673 necessary in the future.

17  
18       674 Despite the aforementioned limitations associated in this study, the present  
19      675 results generated BDNF concentration gradient, condition of which is necessary  
20      676 for hPSC-derived ONPs to differentiate into the otic lineage (i.e., SGNs) and  
21      677 also promoted directional neurite extension towards the POD-BDNF disk. The  
22      678 technique will allow us to control neurite direction of transplanted hPSC-derived  
23      679 ONPs in the inner ear. We will harness this method in our design of a bioactive  
24      680 CI.  
25  
26

27  
28       681 **Conclusions**  
29  
30  
31

32  
33       682 We were able to generate BDNF concentration gradient, enabling survival,  
34      683 neuronal differentiation toward SGNs, and directed neurite extension of hPSC-  
35      684 derived ONPs. The technique will allow us to control neurite direction of trans-  
36      685 planted hPSC-derived ONPs in the inner ear. This proof-of-concept study pro-  
37      686 vides a step toward next-generation bioacitve CI technology.  
38  
39  
40  
41  
42  
43

44  
45       687 **Acknowledgment**  
46  
47

48       688 This work was supported by the American Otological Society Clinician Sci-  
49      689 entist Award (AJM), the Triological Society/American College of Surgeons  
50      690 Clinician Scientist Award (AJM), the Department of Otolaryngology of North-  
51      691 western University (AJM), the NIH (NIDCD) K08 Clinician Scientist Award  
52      692 K08DC13829-02 (AJM), and the Office of the Assistant Secretary of Defense of  
53      693 Health Affairs through the Hearing Restoration Research Program (Award #:  
54  
55  
56  
57  
58  
59  
60  
61  
62  
63  
64  
65

1  
2  
3  
4  
5  
6  
7  
8  
9       694 RH170013:WU81XWUH-18-0712). Imaging work was performed at the North-  
10      695 western University Center for Advanced Microscopy, which is generously sup-  
11      696 ported by NCI CCSG P30 CA060553 awarded to the Robert H. Lurie Com-  
12      697 prehensive Cancer Center, for which we thank Peter Dluhy, Constadina Ar-  
13      698 vanitis, Ph.D., David Kirchenbuechler, Ph.D., and Wensheng (Wilson) Liu,  
14      699 M.D. Some of microfluidic device experiments were performed in the Analytical  
15      700 bioNanoTechnology (ANTEC) Core Facility of the Simpson Querrey Institute  
16      701 at Northwestern University, which is supported by the Soft and Hybrid Nan-  
17      702 otechnology Experimental (SHyNE) Resource (NSFECCS-1542205). We thank  
18      703 Shreyas Bharadwaj (Cornell University), Kyle Coots (Midwestern University),  
19      704 Andrew Oleksijew (the University of Nebraska), Duncan Chadly (California In-  
20      705 stitute of Technology), and Shun Kobayashi (the University of Texas at Austin)  
21      706 for their contribution to the earlier phases of this project. We thank Sara Dun-  
22      707 lop (Department of Neurology, Northwestern University), and Dr. Jacqueline  
23      708 Bond (the University of California San Diego) for assistance in Western Blot and  
24      709 SDS-Page gels. We also thank Dr. Georgia Minakaki (Department of Neurol-  
25      710 ogy, Northwestern University) on assistance in ELISA. Finally, our thanks and  
26      711 appreciation go to our collaborator, Dr. Christian Pernstich (Cell Guidance  
27      712 Systems), for continuous support and stimulating discussions on this project  
28      713 since 2015.  
29  
30  
31  
32  
33  
34  
35  
36  
37  
38  
39  
40  
41

42       714 **References**  
43  
44  
45  
46  
47  
48  
49  
50  
51  
52  
53  
54  
55  
56  
57  
58  
59  
60  
61  
62  
63  
64  
65

- 715      [1] J. G. Naples, M. J. Ruckenstein, Cochlear Implant., Otolaryngologic Clinics  
716      of North America 53 (1) (2020) 87–102. doi:10.1016/j.otc.2019.09.  
717      004.
- 718      [2] B. S. Wilson, M. F. Dorman, Cochlear implants: A remarkable past  
719      and a brilliant future, Hearing Research 242 (1-2) (2008) 3–21. arXiv:  
720      NIHMS150003, doi:10.1016/j.heares.2008.06.005.
- 721      [3] C. Frick, M. Müller, U. Wank, A. Tropitzsch, B. Kramer, P. Senn, H. Rask-  
722      Anderson, K. H. Wiesmüller, H. Löwenheim, Biofunctionalized peptide-

- 1  
2  
3  
4  
5  
6  
7  
8  
9        723 based hydrogels provide permissive scaffolds to attract neurite outgrowth  
10      724 from spiral ganglion neurons, *Colloids and Surfaces B: Biointerfaces* 149  
11      725 (2017) 105–114. doi:10.1016/j.colsurfb.2016.10.003.
- 12  
13  
14        726 [4] S. Hahnewald, A. Tscherter, E. Marconi, J. Streit, H. R. Widmer, C. Gar-  
15        727 nham, H. Benav, M. Mueller, H. Löwenheim, M. Roccio, P. Senn, Response  
16        728 profiles of murine spiral ganglion neurons on multi-electrode arrays., *Jour-*  
17        729 *nal of neural engineering* 13 (1) (2016) 16011. doi:10.1088/1741-2560/  
18        730 13/1/016011.
- 19  
20  
21  
22  
23        731 [5] R. K. Shepherd, S. Hatsushika, G. M. Clark, Electrical stimulation of  
24        732 the auditory nerve: The effect of electrode position on neural excitation,  
25        733 *Hearing Research* 66 (1) (1993) 108–120. doi:10.1016/0378-5955(93)  
26        734 90265–3.
- 27  
28  
29  
30        735 [6] M. Tykocinski, L. T. Cohen, B. C. Pyman, T. Roland, C. Treaba, J. Pal-  
31        736 amara, M. C. Dahm, R. K. Shepherd, J. Xu, R. S. Cowan, N. L. Cohen,  
32        737 G. M. Clark, Comparison of electrode position in the human cochlea using  
33        738 various perimodiolar electrode arrays., *The American journal of otology*  
34        739 21 (2) (2000) 205–211. doi:10.1016/S0196-0709(00)80010-1.
- 35  
36  
37  
38        740 [7] A. Roemer, U. Köhl, O. Majdani, S. Klöß, C. Falk, S. Haumann, T. Lenarz,  
39        741 A. Kral, A. Warnecke, Biohybrid cochlear implants in human neurosensory  
40        742 restoration., *Stem cell research and therapy* 7 (1) (2016) 148. doi:10.  
41        743 1186/s13287-016-0408-y.
- 42  
43  
44  
45        744 [8] R. A. Heuer, K. T. Nella, H. T. Chang, K. S. Coots, A. M. Oleksijew,  
46        745 C. B. Roque, L. H. Silva, T. L. McGuire, K. Homma, A. J. Matsuoka,  
47        746 Three-dimensional otic neuronal progenitor spheroids derived from human  
48        747 embryonic stem cells, *Tissue Engineering - Part A* 27 (3-4) (2021) 256–269.  
49        748 doi:10.1089/ten.tea.2020.0078.
- 50  
51  
52  
53  
54        749 [9] H.-T. Chang, R. A. Heuer, A. M. Oleksijew, K. S. Coots, C. B. Roque, K. T.  
55        750 Nella, T. L. McGuire, A. J. Matsuoka, An Engineered Three-Dimensional

- 1  
2  
3  
4  
5  
6  
7  
8  
9        751 Stem Cell Niche in the Inner Ear by Applying a Nanofibrillar Cellulose  
10      752 Hydrogel with a Sustained-Release Neurotrophic Factor Delivery System,  
11      753 *Acta Biomaterialia* 108 (2020) 111–127. doi:<https://doi.org/10.1016/j.actbio.2020.03.007>.
- 12  
13  
14  
15        755 [10] L. Taylor, L. Jones, M. H. Tuszyński, A. Blesch, Neurotrophin-3 gradients  
16      756 established by lentiviral gene delivery promote short-distance axonal bridg-  
17      757 ing beyond cellular grafts in the injured spinal cord, *Journal of Neuroscience*  
18      758 26 (38) (2006) 9713–9721. doi:[10.1523/JNEUROSCI.0734-06.2006](https://doi.org/10.1523/JNEUROSCI.0734-06.2006).
- 19  
20  
21        759 [11] P. Senn, M. Roccio, S. Hahnewald, C. Frick, M. Kwiatkowska, M. Ishikawa,  
22      760 P. Bako, H. Li, F. Edin, W. Liu, H. Rask-Andersen, I. Pyykkö, J. Zou,  
23      761 M. Mannerström, H. Keppner, A. Homsy, E. Laux, M. Llera, J. P. Lel-  
24      762 louche, S. Ostrovsky, E. Banin, A. Gedanken, N. Perkas, U. Wank, K. H.  
25      763 Wiesmüller, P. Mistrík, H. Benav, C. Garnham, C. Jolly, F. Gander, P. Ul-  
26      764 rich, M. Müller, H. Löwenheim, NANOCI-Nanotechnology Based Cochlear  
27      765 Implant with Gapless Interface to Auditory Neurons, *Otology and Neuro-*  
28      766 *tology* 38 (8) (2017) e224—e231. doi:[10.1097/MAO.0000000000001439](https://doi.org/10.1097/MAO.0000000000001439).
- 29  
30  
31        767 [12] G. J. Goodhill, H. Baier, Axon Guidance: Stretching Gradients to  
32      768 the Limit, *Neural Computation* 10 (3) (1998) 521–527. doi:[10.1162/089976698300017638](https://doi.org/10.1162/089976698300017638).
- 33  
34        770 [13] L. N. Gillespie, G. M. Clark, P. F. Bartlett, P. L. Marzella, BDNF-induced  
35      771 survival of auditory neurons *in vivo*: Cessation of treatment leads to ac-  
36      772 celerated loss of survival effects, *Journal of Neuroscience Research* 71 (6)  
37      773 (2003) 785–790. doi:[10.1002/jnr.10542](https://doi.org/10.1002/jnr.10542).
- 38  
39        774 [14] L. N. Pettingill, R. L. Minter, R. K. Shepherd, Schwann cells geneti-  
40      775 cally modified to express neurotrophins promote spiral ganglion neuron  
41      776 survival *in vitro*, *Neuroscience* 152 (3) (2008) 821–828. doi:[10.1016/j.neuroscience.2007.11.057](https://doi.org/10.1016/j.neuroscience.2007.11.057).Schwann.
- 42  
43        778 [15] R. K. Shepherd, A. Coco, S. B. Epp, Neurotrophins and electrical stim-  
44      779 ulation for protection and repair of spiral ganglion neurons following

- 1  
2  
3  
4  
5  
6  
7  
8  
9        780 sensorineural hearing loss, Hearing Research 242 (2009) 100–109. doi:  
10        781 10.1016/j.heares.2007.12.005.Neurotrophins.  
11  
12  
13        782 [16] B. Baseri, J. J. Choi, T. Deffieux, G. Samiotaki, Y. S. Tung, O. Olu-  
14        783 molade, S. A. Small, B. Morrison, E. E. Konofagou, Activation of sig-  
15        784 naling pathways following localized delivery of systemically administered  
16        785 neurotrophic factors across the bloodbrain barrier using focused ultra-  
17        786 sound and microbubbles, Physics in Medicine and Biology 57 (7). doi:  
18        787 10.1088/0031-9155/57/7/N65.  
19  
20  
21  
22  
23        788 [17] K. Ikeda, S. Nagaoka, S. Winkler, K. Kotani, H. Yagi, K. Nakanishi,  
24        789 S. Miyajima, J. Kobayashi, H. Mori, Molecular Characterization of Bom-  
25        790 byx mori Cytoplasmic Polyhedrosis Virus Genome Segment 4, Journal of  
26        791 Virology 75 (2) (2001) 988–995. doi:10.1128/jvi.75.2.988-995.2001.  
27  
28  
29  
30        792 [18] T. Suzuki, T. Kanaya, H. Okazaki, K. Ogawa, A. Usami, H. Watanabe,  
31        793 K. Kadono-Okuda, M. Yamakawa, H. Sato, H. Mori, S. Takahashi, K. Oda,  
32        794 Efficient protein production using a Bombyx mori nuclear polyhedrosis  
33        795 virus lacking the cysteine proteinase gene, Journal of General Virology  
34        796 78 (12) (1997) 3073–3080. doi:10.1099/0022-1317-78-12-3073.  
35  
36  
37  
38        797 [19] H. Mori, R. Ito, H. Nakazawa, M. Sumida, F. Matsubara, Y. Minobe,  
39        798 Expression of Bombyx mori cytoplasmic polyhedrosis virus polyhedrin in  
40        799 insect cells by using a baculovirus expression vector, and its assembly into  
41        800 polyhedra, Journal of General Virology 74 (1) (1993) 99–102. doi:10.  
42        801 1099/0022-1317-74-1-99.  
43  
44  
45  
46  
47        802 [20] S. H. Green, E. Bailey, Q. Wang, R. L. Davis, The Trk A, B, C's of  
48        803 Neurotrophins in the Cochlea., Anatomical record (Hoboken, N.J. : 2007)  
49        804 295 (11) (2012) 1877–1895. doi:10.1002/ar.22587.  
50  
51  
52  
53        805 [21] I. Meyvantsson, D. J. Beebe, Cell culture models in microfluidic systems,  
54        806 Annual Review of Analytical Chemistry 1 (1) (2008) 423–449. doi:10.  
55        807 1146/annurev.anchem.1.031207.113042.  
56  
57  
58  
59  
60  
61  
62  
63  
64  
65

- 1  
2  
3  
4  
5  
6  
7  
8  
9       [22] Z.-J. Guo, M.-H. Yu, X.-Y. Dong, W.-L. Wang, T. Tian, X.-Y. Yu, X.-D.  
10      Tang, Protein composition analysis of polyhedra matrix of *Bombyx mori*  
11      nucleopolyhedrovirus (BmNPV) showed powerful capacity of polyhedra to  
12      encapsulate foreign proteins., *Scientific reports* 7 (1) (2017) 8768. doi:  
13      10.1038/s41598-017-08987-8.  
14  
15  
16  
17       [23] A. J. Matsuoka, Z. A. Sayed, N. Stephanopoulos, E. J. Berns, A. R. Wad-  
18      hwani, Z. D. Morrissey, D. M. Chadly, S. Kobayashi, A. N. Edelbrock,  
19      T. Mashimo, C. A. Miller, T. L. McGuire, S. I. Stupp, J. A. Kessler,  
20      Creating a stem cell niche in the inner ear using self-assembling peptide  
21      amphiphiles., *Plos One* 12 (12) (2017) e0190150. doi:10.1371/journal.  
22      pone.0190150.  
23  
24  
25  
26  
27       [24] A. J. Matsuoka, Z. D. Morrissey, C. Zhang, K. Homma, A. Belmadani,  
28      C. A. Miller, D. M. Chadly, S. Kobayashi, A. N. Edelbrock, M. Tanaka-  
29      Matakatsu, D. S. Whitlon, L. Lyass, T. L. McGuire, S. I. Stupp, J. A.  
30      Kessler, Directed Differentiation of Human Embryonic Stem Cells Toward  
31      Placode-Derived Spiral Ganglion-Like Sensory Neurons, *Stem Cells Trans-  
32      lational Medicine* 6 (2017) 923–936. doi:10.1002/sctm.16-0032.  
33  
34  
35  
36  
37       [25] H. Al-Ali, S. R. Beckerman, J. L. Bixby, V. P. Lemmon, In vitro models  
38      of axon regeneration, *Experimental Neurology* 287 (Pt 3) (2017) 423–434.  
39      doi:10.1016/j.expneurol.2016.01.020.  
40  
41  
42       [26] U. K. Laemmli, Cleavage of structural proteins during the assembly of  
43      the head of bacteriophage T4., *Nature* 227 (5259) (1970) 680–685. doi:  
44      10.1038/227680a0.  
45  
46  
47       [27] A. L. Mandel, H. Ozdener, V. Utermohlen, Identification of pro- and mature  
48      brain-derived neurotrophic factor in human saliva., *Archives of oral biology*  
49      54 (7) (2009) 689–695. doi:10.1016/j.archoralbio.2009.04.005.  
50  
51  
52  
53       [28] C. A. Schneider, W. S. Rasband, K. W. Eliceiri, NIH Image to ImageJ:  
54      25 years of image analysis, *Nature Methods* 9 (7) (2012) 671–675. arXiv:  
55      arXiv:1011.1669v3, doi:10.1038/nmeth.2089.  
56  
57  
58  
59  
60  
61  
62  
63  
64  
65

- 1  
2  
3  
4  
5  
6  
7  
8  
9        [29] R. W. Burry, Controls for immunocytochemistry: an update., *The journal*  
10      of histochemistry and cytochemistry : official journal of the Histochemistry  
11      Society 59 (1) (2011) 6–12. doi:10.1369/jhc.2010.956920.  
12  
13  
14        [30] M. B. Mazalan, M. A. B. Ramlan, J. H. Shin, T. Ohashi, Effect of geomet-  
15      ric curvature on collective cell migration in tortuous microchannel devices,  
16      *Micromachines* 11 (7) (2020) 1–17. doi:10.3390/MI11070659.  
17  
18  
19        [31] F. Xu, T. Beyazoglu, E. Hefner, U. A. Gurkan, U. Demirci, Automated  
20      and adaptable quantification of cellular alignment from microscopic images  
21      for tissue engineering applications, *Tissue Engineering - Part C: Methods*  
22      17 (6) (2011) 641–649. doi:10.1089/ten.tec.2011.0038.  
23  
24  
25  
26  
27        [32] E. Batschelet, *Circular Statistics in Biology (Mathematics in Biology Series)*,  
28      1st Edition, Academic Press, New York, NY, 1981.  
29  
30  
31        [33] P. Berens, M. J. Velasco, CircStat for Matlab: Toolbox for circular statistics  
32      with Matlab, Max–Planck–Institut f ur biologische Kybernetik, Technical  
33      Report No. 184 31 (10) (2009) 1–21. doi:doi:10.18637/jss.v031.i10.  
34  
35  
36        [34] M. Pool, J. Thiemann, A. Bar-Or, A. E. Fournier, NeuriteTracer: A novel  
37      ImageJ plugin for automated quantification of neurite outgrowth, *Journal*  
38      of Neuroscience Methods 168 (1) (2008) 134–139. doi:10.1016/j.  
39      jneumeth.2007.08.029.  
40  
41  
42        [35] E. Meijering, M. Jacob, J.-C. F. Sarria, P. Steiner, H. Hirling, M. Unser,  
43      Design and validation of a tool for neurite tracing and analysis in fluo-  
44      rescence microscopy images., *Cytometry. Part A : the journal of the*  
45      International Society for Analytical Cytology
- 46      58 (2) (2004) 167–176. doi:  
47      10.1002/cyto.a.20022.  
48  
49  
50  
51  
52        [36] M. Anniko, W. Arnold, T. Stigbrand, A. Strom, The Human Spiral Gan-  
53      glion, *ORL* 57 (1995) 68–77.  
54  
55  
56  
57  
58  
59  
60  
61  
62  
63  
64  
65

- 1  
2  
3  
4  
5  
6  
7  
8  
9        [37] S. van der Walt, S. C. Colbert, G. Varoquaux, The NumPy Array: A  
10      Structure for Efficient Numerical Computation, Computing in Science En-  
11      gineering 13 (2) (2011) 22–30. doi:10.1109/MCSE.2011.37.  
12  
13  
14        [38] J. D. Hunter, Matplotlib: A 2D Graphics Environment, Computing in  
15      Science Engineering 9 (3) (2007) 90–95. doi:10.1109/MCSE.2007.55.  
16  
17  
18        [39] P. Virtanen, R. Gommers, T. E. Oliphant, M. Haberland, T. Reddy,  
19      D. Cournapeau, E. Burovski, P. Peterson, W. Weckesser, J. Bright, S. J.  
20      van der Walt, M. Brett, J. Wilson, K. J. Millman, N. Mayorov, A. R. J.  
21      Nelson, E. Jones, R. Kern, E. Larson, C. J. Carey, I. Polat, Y. Feng,  
22      E. W. Moore, J. VanderPlas, D. Laxalde, J. Perktold, R. Cimrman, I. Hen-  
23      riksen, E. A. Quintero, C. R. Harris, A. M. Archibald, A. H. Ribeiro,  
24      F. Pedregosa, P. van Mulbregt, SciPy 1.0: fundamental algorithms for  
25      scientific computing in Python., Nature methods 17 (3) (2020) 261–272.  
26      doi:10.1038/s41592-019-0686-2.  
27  
28  
29  
30  
31  
32  
33        [40] P. Berens, CircStat : A MATLAB Toolbox for Circular Statistics , Journal  
34      of Statistical Software 31 (10). doi:10.18637/jss.v031.i10.  
35  
36  
37        [41] M. Tuncel, H. S. Sürütçü, K. M. Erbil, A. Konan, Formation of the cochlear  
38      nerve in the modiolus of the guinea pig and human cochleae., Archives of  
39      medical research 36 (5) (2005) 436–40. doi:10.1016/j.arcmed.2005.02.  
40  
41      003.  
42  
43  
44        [42] B. Küçük, K. Abe, T. Ushiki, Y. Inuyama, S. Fukuda, Kazuo Ishikawa,  
45      Microstructures of the Bony Modiolus in the Human Cochlea : A Scanning  
46      Electron Microscopic Study, Journal of Electron Microsc 40 (40) (1991)  
47      193–197.  
48  
49  
50  
51        [43] O. Levenspiel, Chemical Reaction Engineering, 3rd Edition, John Wiley  
52      and Sons, Inc., New York, NY, 1999.  
53  
54  
55        [44] M. Stroh, W. R. Zipfel, R. M. Williams, S. C. Ma, W. W. Webb, W. M.  
56      Saltzman, Multiphoton microscopy guides neurotrophin modification with  
57  
58  
59  
60  
61  
62  
63  
64  
65

- 1  
2  
3  
4  
5  
6  
7  
8  
9        891 poly(ethylene glycol) to enhance interstitial diffusion, Nature Materials  
10      892 3 (7) (2004) 489–494. doi:10.1038/nmat1159.
- 12      893 [45] S. Axler, Linear Algebra Done Right, 3rd Edition, Springer Publishing,  
13      894 New York, NY, 2015.
- 16      895 [46] J. Crank, The mathematics of Diffusion, 2nd Edition, Oxford University  
17      896 Press, London, UK, 1979.
- 20      897 [47] K. M. Keefe, I. S. Sheikh, G. M. Smith, Targeting Neurotrophins to Specific  
21      898 Populations of Neurons: NGF, BDNF, and NT-3 and Their Relevance  
22      899 for Treatment of Spinal Cord Injury., International journal of molecular  
23      900 sciences 18 (3). doi:10.3390/ijms18030548.
- 27      901 [48] B. I. Awad, M. A. Carmody, M. P. Steinmetz, Potential role of growth  
28      902 factors in the management of spinal cord injury., World Neurosurgery 83 (1)  
30      903 (2015) 120–131. doi:10.1016/j.wneu.2013.01.042.
- 32      904 [49] E. R. n. Hollis, M. H. Tuszyński, Neurotrophins: potential therapeutic tools  
33      905 for the treatment of spinal cord injury., Neurotherapeutics : the journal of  
34      906 the American Society for Experimental NeuroTherapeutics 8 (4) (2011)  
35      907 694–703. doi:10.1007/s13311-011-0074-9.
- 39      908 [50] A. H. Nagahara, B. R. Wilson, I. Ivasyk, I. Kovacs, S. Rawalji, J. R.  
40      909 Bringas, P. J. Piviroto, W. S. Sebastian, L. Samaranch, K. S. Bankiewicz,  
41      910 M. H. Tuszyński, MR-guided delivery of AAV2-BDNF into the entorhi-  
42      911 nal cortex of non-human primates., Gene therapy 25 (2) (2018) 104–114.  
43      912 doi:10.1038/s41434-018-0010-2.
- 47      913 [51] S. D. Croll, C. Suri, D. L. Compton, M. V. Simmons, G. D. Yan-  
48      914 copoulos, R. M. Lindsay, S. J. Wiegand, J. S. Rudge, H. E. Scharfman,  
49      915 Brain-derived neurotrophic factor transgenic mice exhibit passive avoid-  
50      916 ance deficits, increased seizure severity and in vitro hyperexcitability in  
51      917 the hippocampus and entorhinal cortex., Neuroscience 93 (4) (1999) 1491–  
52      918 1506. doi:10.1016/s0306-4522(99)00296-1.

- 1  
2  
3  
4  
5  
6  
7  
8  
9        [52] A. Dravid, S. Parittotokkaporn, Z. Aqrawe, S. J. O'Carroll, D. Svirskis,  
10      Determining Neurotrophin Gradients in Vitro to Direct Axonal Outgrowth  
11      following Spinal Cord Injury, ACS Chemical Neuroscience 11 (2) (2020)  
12      121–132. doi:10.1021/acschemneuro.9b00565.  
13  
14  
15  
16        [53] T. Yamagata, J. M. Miller, M. Ulfendahl, N. P. Olivius, R. A. Altschuler,  
17      I. Pyykkö, G. Bredberg, Delayed neurotrophic treatment preserves nerve  
18      survival and electrophysiological responsiveness in neomycin-deafened  
19      guinea pigs., Journal of neuroscience research 78 (1) (2004) 75–86. doi:  
20      10.1002/jnr.20239.  
21  
22  
23  
24        [54] M. P. Zanin, M. Hellstr??m, R. K. Shepherd, A. R. Harvey, L. N. Gillespie,  
25      Development of a cell-based treatment for long-term neurotrophin expres-  
26      sion and spiral ganglion neuron survival, Neuroscience 277 (2014) 690–699.  
27  
28        [55] M. Seyyedi, L. Viana, J. J. Nadol, Within-subject comparison of word  
29      recognition and spiral ganglion cell count in bilateral cochlear implant  
30      recipients, Otol Neurotol 35 (8) (2014) 1446–1450. doi:10.1097/MAO.  
31      000000000000443.Within-Subject.  
32  
33  
34  
35  
36  
37  
38        [56] A. Henriques, C. Pitzer, A. Schneider, Neurotrophic growth factors for the  
39      treatment of amyotrophic lateral sclerosis: where do we stand?, Frontiers  
40      in neuroscience 4 (2010) 32. doi:10.3389/fnins.2010.00032.  
41  
42  
43  
44        [57] J. F. Poduslo, G. L. Curran, Permeability at the blood-brain and  
45      blood-nerve barriers of the neurotrophic factors: NGF, CNTF, NT-3,  
46      BDNF, Molecular Brain Research 36 (2) (1996) 280–286. doi:10.1016/  
47      0169-328X(95)00250-V.  
48  
49  
50  
51        [58] T. Sakane, W. M. Pardridge, Carboxyl-directed pegylation of brain-derived  
52      neurotrophic factor markedly reduces systemic clearance with minimal loss  
53      of biologic activity (1997). doi:10.1023/A:1012117815460.  
54  
55  
56  
57  
58  
59  
60  
61  
62  
63  
64  
65

- [59] R. G. Soderquist, E. D. Milligan, E. M. Sloane, J. A. Harrison, K. K. Douvas, J. M. Potter, T. S. Hughes, R. A. Chavez, K. Johnson, L. R. Watkins, M. J. Mahoney, PEGylation of brain-derived neurotrophic factor for preserved biological activity and enhanced spinal cord distribution., Journal of biomedical materials research. Part A 91 (3) (2009) 719–729.  
doi:10.1002/jbm.a.32254.

[60] M. Sasi, B. Vignoli, M. Canossa, R. Blum, Neurobiology of local and inter-cellular BDNF signaling, Pflugers Archiv : European journal of physiology 469 (5-6) (2017) 593–610. doi:10.1007/s00424-017-1964-4.

[61] X. Li, Y. Su, S. Liu, L. Tan, X. Mo, S. Ramakrishna, Encapsulation of proteins in poly(l-lactide-co-caprolactone) fibers by emulsion electro-spinning, Colloids and Surfaces B: Biointerfaces 75 (2) (2010) 418–424.  
doi:10.1016/j.colsurfb.2009.09.014.

[62] E. E. L. Swan, M. Peppi, Z. Chen, K. M. Green, J. E. Evans, M. J. McKenna, M. J. Mescher, S. G. Kujawa, W. F. Sewell, Proteomics analysis of perilymph and cerebrospinal fluid in mouse., The Laryngoscope 119 (5) (2009) 953–958. doi:10.1002/lary.20209.

[63] T. Numakawa, S. Suzuki, E. Kumamaru, N. Adachi, M. Richards, H. Kunugi, BDNF function and intracellular signaling in neurons, Histology and Histopathology 25 (2) (2010) 237–258. doi:10.14670/HH-25.237.

[64] C. Gentile, Engineering of Spheroids for Stem Cell Technology, Current Stem Cell Research & Therapy 11 (2016) 652–665. doi:10.2174/1574888x10666151001114848.

[65] H. Berg, Random Walks in Biology, Princeton Universtiy Press, Prinston, NJ, 1983.

[66] H. Li, F. Edin, H. Hayashi, O. Gudjonsson, N. Danckwardt-Lilliestr??m, H. Engqvist, H. Rask-Andersen, W. Xia, Guided growth of auditory neu-

1  
2  
3  
4  
5  
6  
7  
8  
9        973        rons: Bioactive particles towards gapless neural electrode interface, Biomaterials 122 (2017) 1–9. doi:10.1016/j.biomaterials.2016.12.020.  
10  
11  
12  
13  
14  
15  
16  
17  
18

19  
20  
21  
22  
23  
24        975        [67] J. Schulze, H. Staeker, D. Wedekind, T. Lenarz, A. Warnecke, Expression  
25        976        pattern of brain-derived neurotrophic factor and its associated receptors:  
26        977        Implications for exogenous neurotrophin application., Hearing Research 413  
27        978        (2020) 108098. doi:10.1016/j.heares.2020.108098.  
28  
29  
30  
31  
32  
33  
34  
35  
36  
37  
38  
39  
40  
41  
42  
43  
44  
45  
46  
47  
48  
49  
50  
51  
52  
53  
54  
55  
56  
57  
58  
59  
60  
61  
62  
63  
64  
65



Click here to access/download  
**Supplementary Material**  
Supplementary\_Data.pdf



Click here to access/download  
**Supplementary Material**  
Supplementary\_Figure\_S1-S10.pdf



Click here to access/download  
**Supplementary Material**  
Supplementary\_Table\_S1-S3.pdf

**Declaration of interests**

The authors declare that they have no known competing financial interests or personal relationships that could have appeared to influence the work reported in this paper.

The authors declare the following financial interests/personal relationships which may be considered as potential competing interests: